



138
545
THS

02206706

This is to certify that the
thesis entitled

MULTI-LAYERED EXPERIMENTAL AND NUMERICAL
ANALYSIS OF STAMP THERMOFORMING PROCESSING
OF NATURAL FIBER REINFORCED POLYPROPYLENE
SHEETS

presented by

BARBARA NICOLE RODGERS

has been accepted towards fulfillment
of the requirements for the

M. S. degree in Mechanical Engineering



Major Professor's Signature

12 / 15 / 04

Date

**MULTI-LAYERED EXPERIMENTAL AND NUMERICAL ANALYSIS OF
STAMP THERMOFORMING PROCESSING OF NATURAL FIBER
REINFORCED POLYPROPYLENE SHEETS**

By

Barbara Nicole Rodgers

A THESIS

Submitted to
Michigan State University
in partial fulfillment of the requirements
for the degree of

MASTER OF SCIENCE

Department of Mechanical Engineering

2004

ABSTRACT

MULTI-LAYERED EXPERIMENTAL AND NUMERICAL ANALYSIS OF STAMP THERMOFORMING PROCESSING OF NATURAL FIBER REINFORCED POLYPROPYLENE SHEETS

By

Barbara Nicole Rodgers

Due to increasing ecological concerns, much attention has been given to the study of natural fiber composites to replace non-biodegradable glass and woven fabric composites. This study focuses predominantly on kenaf natural fibers with a polypropylene matrix. The first objective was to produce a fabrication process that yielded composites with comparable properties to existing synthetic fiber composites. A detailed outline of this optimized process for compression moulding is presented. In addition, material characterization was done which included squeeze flow, tensile, and flexural testing. The results show that this newly developed fabrication process produced composites with competitive flexural and tensile strength to other natural fiber composites both using compression moulding and other fabrication processes.

The fabricated kenaf/polypropylene composites were then formed using a stamp thermo-forming press. The material showed good formability. In addition, numerical analysis was done which included single and double layered modeling. An updated material law constitutive relationship for multiple preferred fiber orientations was used to model the laminae, while two interface models were used: linear softening and plasticity. Additional research was done on other possible material and interface models to be used in the future.

DEDICATION

"I can do all things through Christ which strengtheneth me." -Philippians 4:13

ACKNOWLEDGMENTS

Thank You!

Giving all honor and glory to God, who is truly the head of my life.

To my beloved parents, I will always be grateful for your years of unconditional love and support.

To my loving husband, who is always right by my side. Without his love this definitely would have been a lot harder to achieve.

Special thanks to my advisor Dr. Farhang Pourboghrat for his leadership and guidance throughout my graduate experience. In addition, thanks to Dr. Michael Zampaloni for being willing to share his expertise in order to help me. Furthermore, to Stacey Yankovich, with whom I worked closely with during this entire process.

This work would also have not been possible without assistance from the Composite Materials and Structures Center at Michigan State University. In particular, Dr. Drzal, Dr. Misra, and Dr. Huda, who were all very helpful in providing information or materials needed to make this research a successful endeavor.

Sincerely,

Barbara Nicole Rodgers

December 2004

East Lansing, Michigan

TABLE OF CONTENTS

LIST OF TABLES	vi
LIST OF FIGURES	vii
ABBREVIATIONS	viii
CHAPTER 1 INTRODUCTION AND LITERATURE REVIEW	1
1.1 Introduction to Biocomposites.....	1
1.2 History of Composite Modeling.....	5
1.2.1 Cohesive Zone Model	6
1.2.2 Continuum Damage Model	9
1.2.3 Rate Dependent Models.....	12
1.2.4...Interface Models	16
CHAPTER 2 BIOCOMPOSITE.....	23
2.1 Fabrication of Kenaf/Polypropylene Composite	23
2.2 Material Characterization – Directionality	29
2.3 Material Characterization – Properties.....	33
2.4 Compression Moulding Process and Composite Comparison.....	38
CHAPTER 3 EXPERIMENTAL WORK	42
3.1 Introduction to Stamp Thermoforming	42
3.2 Experimental Stamping Results.....	44
CHAPTER 4 NUMERICAL ANALYSIS.....	47
4.1 Material Model	47
4.2 Numerical Stamping Results.....	50
4.2.1 Two Preferred Fiber Orientations	50
4.2.2 Three Preferred Fiber Orientations	57
4.2.3 Four Preferred Fiber Orientations	59
4.3 Discussion of Results	62
CHAPTER 5 CONCLUSIONS.....	69
CHAPTER 6 FUTURE WORK.....	70
BIBLIOGRAPHY	71

LIST OF TABLES

Table 1. Plasticity model properties of the interface	20
Table 2. Tensile testing results for all specimens – Young’s Modulus.....	35
Table 3. Tensile testing results for all specimens – Poisson’s Ratio	36
Table 4. Flex testing results for all specimens – Modulus of Elasticity	37
Table 5. Material properties for simulation	37
Table 6. Sensitivity analysis of Young’s Modulus.....	61

LIST OF FIGURES

Figure 1. Linear function of pressure-overclosure relationship	18
Figure 2. (a) Carver Press (b) Tetrahedron Press	24
Figure 3. Long Kenaf fibers sandwiched between two PP sheets	25
Figure 4. Chopped Kenaf fibers sandwiched between two PP sheets	25
Figure 5. Premixed chopped Kenaf fibers and PP.....	25
Figure 6. Multilayered composite fabrication process.....	26
Figure 7. Multilayered fabricated composite.....	27
Figure 8. Squeeze flow test sample before testing	29
Figure 9. Schematic of squeeze flow test experimental setup [27].....	30
Figure 10. Squeeze flow test sample after testing.....	30
Figure 11. Normalized length versus angle for all samples.....	31
Figure 12. Normalized length versus angle for best samples	32
Figure 13. Kenaf/PP and PP tensile specimens	33
Figure 14. Stress strain curve for 40° fiber orientation specimens at room temperature	34
Figure 15. Stress strain curve for 170° fiber orientation specimens at room temperature	34
Figure 16. Stress strain curve for Polypropylene/Epolene specimens at room temperature	35
Figure 17. Tensile strength comparison	39
Figure 18. Flexural strength comparison	39
Figure 19. Flexural strength comparison for various manufacturing processes	40

Figure 20. Modulus per cost comparison	41
Figure 21. Specific modulus comparison.....	41
Figure 22. Stamp thermo-hydroforming press	42
Figure 23. Stamp thermoforming schematic	43
Figure 24. Stamp thermoformed part with tearing - top view	44
Figure 25. Stamp thermoformed part A, (a) top view, (b) side view.....	45
Figure 26. Stamp thermoformed part B, (a) top view, (b) side view.....	45
Figure 27. Stamp thermoformed part C, (a) top view, (b) side view.....	46
Figure 28. Deformed blank for $v=0.2$ (a) $V_f=0.218$ (b) $V_f=0.384$ (c) $V_f=0.6$	53
Figure 29. Deformed blank for $v=0.3$ (a) $V_f=0.218$ (b) $V_f=0.384$ (c) $V_f=0.6$	54
Figure 30. Deformed blank for $v=0.4$ (a) $V_f=0.218$ (b) $V_f=0.384$ (c) $V_f=0.6$	55
Figure 31. Deformed blank for $v=0.3$ and $V_f=0.384$ with a plasticity model interface.....	56
Figure 32. Deformed blank for 3 preferred fiber orientations VUMAT	57
Figure 33. Stress contour plot for 3 preferred fiber orientations VUMAT	57
Figure 34. Internal (a) and Kinetic (b) energy plots for 3 preferred fiber orientations VUMAT.....	58
Figure 35. Deformed blank for 4 preferred fiber orientations VUMAT	59
Figure 36. Stress contour plot for 4 preferred fiber orientations VUMAT.....	59
Figure 37. Internal (a) and Kinetic (b) energy plots for 4 preferred fiber orientations VUMAT.....	60
Figure 38. Front angled views of formed part and simulations	62
Figure 39. Top views of experimental and simulation results	63

ABBREVIATIONS

P_i . – Force

K_{ij} . – Diagonal Matrix of Penalty Stiffnesses

D_j . – Displacement

F. – Load Surface

$f(P)$. – Normalized measure of P

P. – Pressure

τ_i . – Interlaminar Direct and Shear Stresses

k_i^0 . – Penalty Stiffnesses of the Interface

δ_j . – Displacements

k_{i0} – Initial Stiffness

k_i – $10^5 \sim 10^7 \text{ mm}^{-1}$

τ_{ic} . – Interlaminar Tensile and Shear Strengths

$f_s(\tau_i)$ – Failure Function

$f_g(G_i)$ – Failure Criterion

G_i – Energy Release Rates

G_I, G_{II}, G_{III} – Critical Energy Release Rates in Mode I, II, and III

$F(\tau_i, G_i)$ – Damage Surface

φ – Function to Control Shrinkage Rate

t – Traction Vector

Γ – Surface

$[u]$ – Vector of Displacement Jumps

K – Elastic Interface Stiffnesses

$f(t,\lambda)$ – Viscoplastic Potential

h – Hardening/Softening Coefficient

τ – Time

N – Model Parameter

$\hat{\gamma}_i$ – Material Parameter

λ – Viscoplastic Multiplier

D_i – Damage Variables

Y_i – Conjugate to Damage Variables

E_{11} – Longitudinal Young's Modulus

E_{22} – Transverse Young's Modulus

E_{ii} – Young's Modulus for i^{th} Fiber Direction

E_f – Young's Modulus of the Fiber

E_m – Young's Modulus of the Matrix

ν_{12}, ν_{21} – Poisson's Ratio

ν_f – Poisson's Ratio of the Fiber

ν_m – Poisson's Ratio of the Matrix

G_{12} – Shear Modulus

G_{13}, G_{23} – Transverse shear Moduli,

G_f – Shear Modulus of the Fiber

G_m – Shear Modulus of the Matrix

N – Number of Plies

[Q] – Stiffness Matrix

[S] – Compliance Matrix

[T(θ)] – Transformation Matrix

θ – Angle between Material Frame and Fiber Directions

\bar{Q}_k – Transformed Reduced Stiffness Matrix

t – Ply Thickness

V_{f0} – Initial Fiber Volume Fraction

V_f – Fiber Volume Fraction

$[\sigma]_k$ – Stress Tensor

$[\epsilon]_k$ – Strain Tensor

ρ – Density of the Composite Material

f_{vd} – Damping Forces

μ_0 – Critical Damping Fraction

m – Nodal Mass

k_e – Nodal Contact Stiffness

$E_{interface}$ – Young's Modulus of the Interface

$G_{interface}$ – Shear Modulus of the Interface

$t_{interface}$ – Thickness of the Interface

$d\epsilon$ – Nominal Strain Increment

σ_t – Elastic Trial Stress

Δt – Relative Displacement

σ_{11} – Normal Stress

σ_y – Yield Stress

E_h – Hardening Modulus of the Interface

$d\varepsilon_{p1}$ – Plastic Strain Increment

k – Thermal Conductivity

T_{master} – Temperature of Master Node

T_{slave} – Temperature of Slave Node

A – Nodal Area

Δt – Stable Time Increment

L^e – Characteristic Element Length

c_d – Dilation Wave Speed of the Material

Chapter 1

INTRODUCTION AND LITERATURE REVIEW

1.1 – Introduction to Biocomposites

In the past few decades, research and engineering has shifted from monolithic materials to fiber-reinforced polymer materials. Although glass fibers are the most widely used reinforcements of plastics due to their low cost and good mechanical properties, they have quite a few drawbacks. These include high density the fact that they are not renewable, recyclable, biodegradable, or CO₂ neutral. These fibers also are abrasive to machines and present a health risk when inhaled. Therefore, natural fibers have come to the forefront in research, and unlike glass fibers, do not share these same shortcomings [1].

In recent years, there have been many discussions about preserving the world's natural resources and recycling. This has led to an interest in the use of biodegradable materials that come from renewable raw materials in composites. A biocomposite consists of a biodegradable polymer as a matrix and a biofibre as reinforcement. In most applications of composites, it is most beneficial to have a matrix that is resilient to the environment, thus, for now, composite research mostly focuses on natural fibers within a non-biodegradable synthetic polymer matrix [2]. While, natural fibers traditionally were used to reinforce thermosets, greater attention is now being placed on using natural fibers to reinforce thermoplastics, such as polypropylene, due to its recyclability [3].

The automobile industry, in particular, is constantly looking for ways to decrease weight and cost of interior and engine components. It is estimated that in the near future polymer and polymer composites will make up 15% of each automobile [4]. Some applications are in the door and instrument panels, glove boxes, package trays, arm rests, and seat backs [5]. These natural fiber composites are an alternative to the wood or glass reinforced composites currently used. The main advantages include low cost, low density, good specific strength, enhanced energy recovery, reduced tool wear and dermal/respiratory irritation, and biodegradability [6]. The disadvantages include a low processing temperature and its general hydrophilic (water absorbent) nature, which is not compatible with hydrophobic (non-water absorbent) polymeric matrices [2]. This problem can be remedied by surface treatment of the fiber or by adding a coupling agent, which will be discussed later in detail. In addition, the use of surface treatments or a coupling agent can enhance the mechanical properties of natural fiber-reinforced composites by ensuring good adhesion between the fiber and the matrix [7].

For this study, the natural fiber chosen was Kenaf with a Polypropylene (PP) matrix. Kenaf fiber (*Hibiscus cannabinus*) is native to Africa and is also grown in the United States in tropical and subtropical regions. The approximate cost of Kenaf bast fibers are 20 – 25 ¢ per pound (40 – 45 ¢ per kg) versus 90¢ per pound (\$2 per kg) for E-glass fiber [7]. Natural fibers characteristics can vary considerably depending on source, age, extraction period and technique, weather variability, and the quality of the soil and climate of the particular region

it is grown in [8]. Yet, studies have shown that fibers from the same batch that contain similar histories grown in moderate conditions result in composites that have low variation in properties. In these conditions, Kenaf fiber can grow as much as 9.8 ft (3 m) in 3 months. Although research has only recently begun to take a serious interest in Kenaf as reinforcement, mankind has used Kenaf even in ancient times as canvas, rope, and sacking [9].

The main constituents of the natural fiber are cellulose, hemicellulose, and lignin. Cellulose is a hydrophilic glucan polymer consisting of linear chains of anhydroglucose units that contain alcoholic hydroxyl groups. This is the reason all natural fibers are hydrophilic: their moisture content reaches 8 – 12.6%. The chemical structure of cellulose is the same for different natural fibers although the degree of polymerization varies, which is related to the mechanical properties of the fiber [6].

The lignin is a biochemical polymer that structurally supports the plant. It is generally resistant to microbial degradation, but surface treatment of the fibers can tend to make it susceptible to the cellulose enzyme. When the plant cell walls are synthesized, cellulose and hemicellulose are present first, and then lignin fills the spaces cementing them together. This process is known as lignification and causes a stiffening of the cell walls in the fiber [2].

Polypropylene (PP) belongs to a class of materials known as polyolefins. These polymers account for approximately 60 % of the total polymer produced. They are so widely used because they have good chemical and physical properties including low cost, good recyclability, and good processibility. Out of

all the polyolefins, polypropylene is known to be one of the most recyclable. Polyolefins are fabricated by various methods including injection moulding, extrusion, compression moulding, injection blow molding, and calendaring into films, fiber, pipe, and sheet products of various shapes and sizes [10].

Polypropylene is a thermoplastic material that is produced by a polymerization process that aligns propylene molecules, or monomer units, into long molecules or chains. This process produces a semicrystalline solid that is characterized by high rigidity, heat resistance, and melting point (~ 157C), low density, and relatively good impact resistance. In the solid state, the properties are dependent upon the amount of crystalline and amorphous regions produced during forming, while, in the melting state, they are determined by the average length of the polymer chains and their distribution in a product. Therefore, the properties can be altered simply by changing the chain lengths, distribution, or by adding a comonomer such as ethylene into the polymer chains or impact modifier into the resin mixture [11]. These properties make polypropylene ideal for use as a matrix in the stamp thermo-hydroforming process.

1.2 – History of Composite Modeling

The finite element analysis of failure in composites has been addressed using many different types of interface elements and interface laws. The most typical mode of interfacial damage in laminated composites is delamination. It occurs between the constituent layers in a composite due to their weak interlaminar strengths. This can happen under various types of loading including transverse concentrated loads in the form of low velocity impacts, which is the case in stamp thermoforming. The initiation of delamination is commonly predicted using stress-based methods, while the propagation of delamination is described using fracture mechanics [16].

When it comes to simulating delamination, or the separation of lamina in composites, there are two model groups – fracture mechanics or damage mechanics/softening plasticity models. If there are no non-linearities in the material behavior, linear elastic fracture mechanics (LEFM) provides an accurate method for prediction of delamination, provided that the initial location of delamination is known. Some examples are the virtual crack closure, virtual crack extension, J-integral, and stiffness derivative methods. The idea is that a critical energy release rate value must be reached before delamination can propagate [17].

These methods are often straight forward for two dimensional analyses since the crack forms and propagates in one direction, which is not the case in three dimensions. In addition, the initial location of crack formation, or flow, is known. Therefore, great effort has been put into developing models that use a

damage mechanics and/or softening plasticity model combined with fracture mechanics to not only capture the initiation of the delamination, but its propagation. This work began with a fictitious crack model (FCM) developed in 1976 by Hillerborg et al. FCM uses a model where stresses act across a crack while it is narrowly opened and introduced fracture mechanics into finite element analysis [18]. This model was the basis for many other models. The models discussed in this study are the cohesive zone model (CZM), the continuum damage model/penalty technique, and rate dependent models.

1.2.1 – Cohesive Zone Model

The history of the cohesive zone model can be traced as far back as 1960 when Dugdale developed a method to trace the spread of plasticity from the center of stress concentration as loads increase. The yielding at the end of a slit in a sheet was investigated to find a relationship between the external load applied and the amount of plastic yielding. In order to verify the accuracy of the model, panels containing both internal and external slits were loaded in tension so that the lengths of the plastic zones could be measured [19]. This model eventually took many different forms. In 2000, Borg et al simulated delamination using the explicit FE code LS-DYNA and a Cohesive Crack Model [20]. In this model, crack propagation was restricted to a known surface and the presumed path was modeled as an adhesive interface initially tying both surfaces (laminae) together. Coincident nodes were used along the interface and the problem was simply reduced to determining a force-displacement relationship between nodes as follows.

$$P_i = K_{ij}D_j \quad (1)$$

In this equation, P is the force, D is displacement, and K is a diagonal matrix of 3 orthogonal springs representing the penalty formulation. This penalty stiffness is valid until a certain combination of these forces is reached then before delamination will propagate. The amount of dissipated energy will shrink the size of the maximum load surface which will in turn reduce the stiffness making it possible for an elastic unloading. The initial maximum load surface is shown below.

$$F = f(P) - 1 = 0 \quad (2)$$

In this equation P is the vector of adhesive forces, and f is the normalized measure of P , force. The function f is determined using an experimental program to assure it approaches unity as the load state reaches its limiting value. The work is validated by using a basic delamination model of two steel cubes, and doing delamination simulations for all 3 modes: double cantilever beam (Model 1), end notch flexural (Mode 2), and mixed mode bending (Mode 3) [20].

Another approach used a cohesive zone model that allows for displacement jumps across a crack represented by extra degrees of freedom at the coincident interface nodes. This model allows for a path of discontinuity that is independent of the mesh structure. There are no restrictions on the type of finite element used and the jumps are continuous across the element boundaries making it more versatile for different meshes [21].

Cohesive zone models can also be used in conjunction with other existing models to simulate different material behaviors. In 2000, Espinosa et al used a

cohesive zone model in conjunction with an anisotropic viscoplastic model to simulate delamination in glass fiber reinforced plastic (GRP) composites. The large deformations in the material are described with the viscoplastic model in Lagrangian coordinates with its coefficients determined experimentally. The interface consisted of zero thickness interface elements that were embedded between the laminae. The tensile and shear tractions of these elements were calculated from interface cohesive laws that described these tractions in terms of normal and tangential displacement jumps. Once the displacements reach a specified critical value, the interface elements fail, and delamination takes place [22].

In recent years, a two-parameter cohesive zone model has emerged. In 2003, this type of model was coupled with finite element analysis to study fracture of fiber composites and adhesively bonded joints. This model was based on fracture models and criteria stating that two parameters exist that describe fracture, i.e. a critical limiting value of maximum stress, σ_{\max} , and fracture energy, G_c . The aim was to determine if the maximum stress values was unique for a given problem or if there was any physical significance to this parameter. Both analytical and finite element analysis was done to validate this model [23].

In 2004, Borg et al used a cohesive zone based delamination model and applied it to a low velocity transverse impact simulation. The purpose was to model delamination initiation and growth with this specific type of deformation. This model was simulated in LS-DYNA and applied to a glass fiber/epoxy three layer cross-ply laminate. The composite was subjected to a non-penetrating

transverse impact using a spherical impactor. In addition, a simulation was done on an eight layer laminate of Carbon fiber. This study improved upon existing models by making it possible to determine the local fiber orientations above and below the interface relative to the propagation direction of the delamination. In addition, an interpolation scheme is used to determine arbitrary energy release rates from a finite number of experiments. Although this was a 2D model, it has very promising results for use in a 3D application [24].

Overall, the cohesive zone model has been shown to be in good agreement with experimental data in all cases. This model is an easier model to implement, and does not require the addition of interface elements since it can also be used with coincident nodes between laminae. It also has shown the ability to be combined with different material models. Disadvantages include the determination of the specific properties used in this model for a specific laminate, and overall implementation in ABAQUS/Explicit, which would require the development of a user subroutine.

1.2.2 – Continuum Damage Model/Penalty Technique

In the continuum damage model a composite laminate is made up of stacked homogeneous isotropic layers. The damage surface is based on fracture mechanics – assuming initial defects/cracks and a stress based failure criterion – which predicts initiation of delamination. A zero thickness layer is used between each lamina that unifies initiation and propagation of the delamination. The interlaminar direct and shear stresses are related to the displacements δ by the constraints of the penalty stiffness of the interface k as follows [16].

$$\tau_i = k_i^0 \delta_i \quad (3)$$

The stiffness is initially very large and displacements are zero to simulate a perfect bond, which degrades as damage increases. The following equation was used to estimate the initial stiffness values.

$$k_i^0 = k_i \tau_{ic} \quad (4)$$

In this equation τ_{1c} , τ_{2c} , and τ_{3c} are the interlaminar tensile and shear strengths and k_i is approximately $10^5 \sim 10^7 \text{ mm}^{-1}$. The maximum displacement before delamination is very small and usually below $10^{-5} \sim 10^{-7} \text{ mm}$. As the loading increases the delamination damage initiates and slowly develops at the interface.

In order to represent micro-defects in the context of continuum damage mechanics, a damage parameter was required. The effective properties of the composite, i.e. stiffness, can then be represented using this damage parameter. The parameter, ω , is 0 when the composite is in an undamaged state and 1 when it is in a fully delaminated state. The tractions are then represented as follows.

$$\tau_i = k_i^0 (1 - \omega) \delta_i \quad (5)$$

This gives the constitutive law for an interface with delamination damage. As the effective stiffness decreases damage grows. The growth is driven by interlaminar stresses according to the appropriate damage law described next.

For the damage surface, conventional stress-based failure criterion is used to predict the initiation of the damage.

$$f_s(\tau_i) - 1 = 0 \quad (6)$$

Here f_s is a failure function which was chosen using appropriate criterion.

$$f_s = \frac{\tau_1^2}{\tau_{1c}^2} + \frac{\tau_2^2}{\tau_{2c}^2} + \frac{\tau_3^2}{\tau_{3c}^2} \text{ if } \tau_1 > 0 \quad (7)$$

Once the delamination exists, fracture mechanics predicts propagation using the failure criterion f_g shown below.

$$f_g(G_i) - 1 = 0 \quad (8)$$

Here, G_i are the energy release rates corresponding to each fracture mode (I, II, III). The function f_g is chosen to have the following form.

$$f_g = \left(\frac{G_I}{G_{IC}} \right)^\alpha + \left(\frac{G_{II}}{G_{IIC}} \right)^\beta + \left(\frac{G_{III}}{G_{IIIC}} \right)^\gamma \quad (9)$$

Where, G_I , G_{II} , and G_{III} are the critical energy release rates in Mode I, II, and III, respectively. This completes a softening interfacial constitutive relationship in which the shrinkage rate can be controlled by a function φ that is a term in the damage surface equation.

$$F(\tau_i, G_i) = f_s(\tau_i) - [1 - \varphi(f_g)] = 0 \quad (10)$$

The damage surface is in the τ_i and G_i space. The function φ is monotonically increasing and satisfies the conditions $\varphi(0) = 0$ and $\varphi(1) = 1$. This allows the damage surface to shrink in the stress space with increasing damage. The damage is irreversible and non-linear. Penetration is also taken into account and if it does occur, the stiffness is returned to the initial value and the interface will not degrade further [16].

This method was coupled with the Lagrange multiplier method in 2003 by Bruno et al. The purpose was to enforce interface displacement continuity

between the plate elements and to determine an accurate and direct approach to evaluate the direct energy release rates [25]. As before, the initial adhesion of both layers before delamination was simulated by treating interface stiffnesses as penalty parameters.

This created an accurate laminate model using multilayer shear deformable plate modeling coupled with interface elements. These elements were used to simulate mixed mode delamination in composites.

1.2.3 – Rate Dependent Models

There were two different rate dependent interface models found in the literature used for composites: a viscoplastic model and a time-dependent elastic damage model. They were used to simulate interface degradation in polymer matrix composites, which includes debonding and rate-dependent delamination. The basic interface model for both consisted of a relationship between the traction vector t relevant to a surface Γ , which divided a solid into two parts, Ω_+ and Ω_- . The vector of displacement jumps between the two parts was represented by $[u]$. The laminate is represented by a stacking sequence of layers and interfaces. The interface is a zero-thickness layer which transfers stress from one layer to the next [26].

The viscoplastic interface model was governed by the following equations.

$$[u] = [u]^e + [u]^{vp} \quad (11)$$

$$t = K[u]^e \text{ where } K = \text{diag}(K_i), i=1,2,3 \quad (12)$$

$$[u]^{vp} = \gamma \langle f(t, \lambda) \rangle_+^N \frac{\partial f(t, \lambda)}{\partial t} \quad (13)$$

$$f(t, \lambda) = \sqrt{a_1 t_1^2 + a_2 t_2^2 + a_3 \langle t_3 \rangle_+^2} - 1 + h\lambda \quad (14)$$

$$\lambda = \int_0^\tau \sqrt{\left(\overset{\circ}{[u]}^{vp} \right)^T \left(\overset{\circ}{[u]}^{vp} \right)} d\tau' \quad (15)$$

$$\langle \bullet \rangle_+ = \bullet \text{ if } \bullet > 0 \quad \langle \bullet \rangle_+ = 0 \text{ if } \bullet \leq 0 \quad (16)$$

Equation 11 shows the addition of the elastic and viscoplastic discontinuities. The elastic portion is governed by equation 12 where K is the elastic interface stiffnesses that relate the traction, t, to the elastic discontinuities. Equation 13 governs the evolution of the viscoplastic displacement discontinuities through a Perzyna kind law, where f (t,λ) is a viscoplastic potential defined by equation 14. Here, the a_i terms are directly related to the values of tractions at the beginning of inelastic behavior, while h relates to the hardening/softening in the model. When h is positive, a softening effect takes place, and the interface degrades. Equation 14 defines the viscoplastic multiplier and contains τ which is time. In both equations, N is a model parameter, λ is a viscoplastic multiplier and t_i are tractions. The final equation, 16, simply shows the meaning of the symbol used for the positive part of what it contains. In equation 14, the positive part of the traction normal to the interface is used to keep viscoplastic displacement discontinuities from developing in the normal direction due to interface compression.

The main characteristics of the viscoplastic model are that it has irreversible viscoplastic displacement discontinuities, an evolution law of the Perzyna kind, a unilateral effect in the normal direction, and a softening behavior

to simulate interface degradation. The model depends on nine parameters as follows where F, L, and T denote force, length, and time, respectively.

$$K_i[F/L^3], i=1,2,3 \quad (17)$$

$$a_i[L^4/F^2], i=1,2,3 \quad (18)$$

$$h[1/L] \quad (19)$$

$$\gamma[F/LT] \quad (20)$$

$$N \quad (21)$$

The time-dependent damage model was an anisotropic time-dependent elastic-damage model with 3 damage variables and is governed by the following equations.

$$t_1 = (1-D_1)K_1[u]_1, \quad t_2 = (1-D_2)K_2[u]_2 \quad (22)$$

$$t_3 = (1-D_3)K_3^+ \langle [u]_3 \rangle_+ + K_3^- \langle [u]_3 \rangle_- \quad (23)$$

$$Y_1 = \frac{1}{2} K_1 [u]_1^2, \quad Y_2 = \frac{1}{2} K_2 [u]_2^2, \quad Y_3 = \frac{1}{2} K_3^+ \langle [u]_3 \rangle_+^2 \quad (24)$$

$$\hat{f}(Y, \lambda) = \sqrt{\hat{a}_1 Y_1 + \hat{a}_2 Y_2 + \hat{a}_3 Y_3} - 1 + \hat{h} \lambda \quad (25)$$

$$\dot{D}_i = \hat{\gamma}_i \left\langle \hat{f}(Y, \lambda) \right\rangle_+^N, \quad i=1,2,3 \quad (26)$$

$$\dot{\lambda} = \sqrt{\sum_{i=1}^3 \dot{D}_i^2} \quad (27)$$

Equations 22 and 23 show the elastic-damage behavior of the interface where K_i are the initial interface stiffnesses and D are the three damage variables for each

mode. The differences in equation 23 for the normal direction are to introduce the elastic behavior in the model depending on the sign of the normal displacement discontinuities. The conjugate to the damage variables, Y_i , are shown in equation 24. Equations 25 – 26 show the evolution of the three damage variables. The first equation, 25, shows the potential function or the amount of accumulated damage, and is dependent on Y and λ . Equation 26 defines the damage variable rates as a function of the positive part of the potential function and the material parameters N and $\hat{\gamma}_i$. Therefore, a softening effect is introduced if and only if the damage variables always increase.

The damage interface model also depends on nine parameters as shown below.

$$K_i[F/L^3], i=1,2,3 \quad (28)$$

$$\hat{a}_i[L/F], i=1,2,3 \quad (29)$$

$$\hat{h} \quad (30)$$

$$\hat{\gamma}[1/T] \quad (31)$$

$$N \quad (32)$$

In summary, the first interface model is viscoplastic with irreversible viscoplastic displacement discontinuities, an evolution law of the Perzyna kind, a unilateral effect in the normal direction, and a softening behavior to simulate the degradation of an interface. The second model is a time-dependent elastic damage model, anisotropic, contains three damage variables, and also a

unilateral effect in the normal direction. This model simulates interface degradation by using an evolution law of damage variables that is governed by a potential function.

The main advantage to using one of these rate-dependent interface models is reduced computing time due to improved time step integration and element formulation. The disadvantages, however, are the extensive number of parameters needed for both models. The problem is in parameter identification for a particular interface. In addition, extensive experimentation must be done to show if the delamination occurring with a particular material is indeed time dependent. Therefore, it has good potential, but it is also hard to implement.

Overall, the models discussed in this literature review were very complex and required many input parameters. In some cases, there was no clear method on how to determine these inputs. Therefore it was established that the use of a less complex model would be beneficial in this study. The models used have input parameters that are common material properties, and were either determined experimentally in this study, or can be in future work.

1.2.4 Interface Models

There were two interface models used in this study, partially because of the simplicity to implement. The first model was a linear softening interface. The linear softening was a built in function in ABAQUS and is defined by a contact pressure-overclosure relationship [28]. There are two main types of contact pressure-overclosure relationships. The first is “hard” contact that minimizes penetration of slave nodes into the master surface and blocks the transfer of

tensile stress across the interface. The second “softened” contact relationship used a contact pressure that is either a linear function, exponential function, or a piecewise linear (tabular) function of the clearance between the surfaces. In addition, a viscous damping relationship can be defined to further affect the interface behavior.

The contact pressure-overclosure relationship chosen was of the “softened” form and was prescribed by a linear law. This “softened” contact pressure-overclosure relationship can be used to model a soft, thin layer on either one or both surfaces. In ABAQUS/Explicit the contact can be enforced using a kinematic or penalty constraint method. The kinematic predictor/correct contact algorithm doesn’t allow any penetrations. Therefore, the penalty contact algorithm is often chosen. Although the enforcement of contact constraints is weaker, it allows for a more general treatment of different types of contact. In addition, with the use of the penalty constraint method, as the contact stiffness increases the time increment decreases. With penalty enforcement, which was used here, the contact collisions are elastic except in the case a contact damping is specified. If this is the case, some energy will be absorbed by the impact. This energy tends to increase as the contact stiffness increases. The damping is defined by a critical damping fraction, which is a unitless damping coefficient in terms of the fraction of critical damping associated with a particular contact stiffness. The damping forces are then calculated as follows.

$$f_{vd} = \mu_0 \sqrt{4mk_e} v_{rel}^{el} \quad (33)$$

Here, the damping force, f_{vd} , is a function of the critical damping fraction, μ_0 , nodal mass, m , nodal contact stiffness, k_e , and the relative rate of motion between the two surfaces, v_{rel}^{el} .

In using the linear pressure-overclosure relationship, the user must define the slope, k , of the relationship. A general graph representing this relationship is shown below.

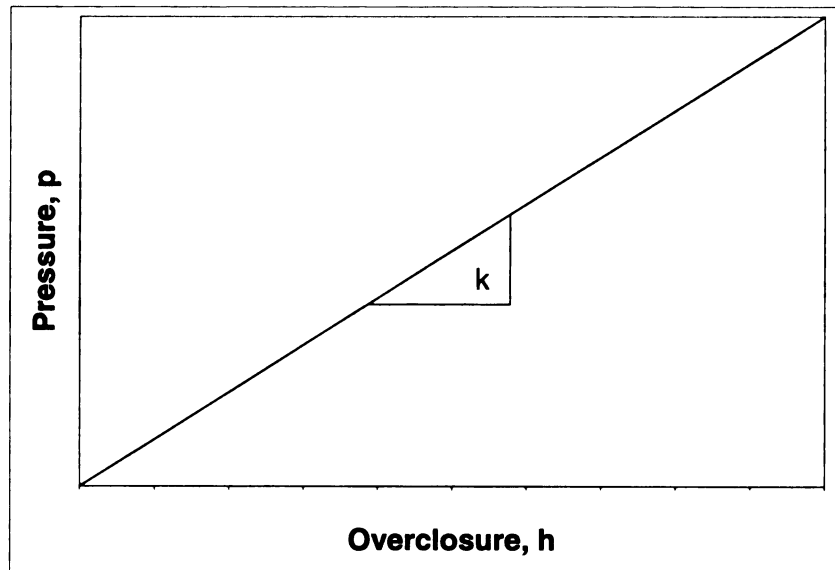


Figure 1. Linear function of pressure-overclosure relationship.

An approximation for the slope of the pressure-overclosure relationship is given in equation 34.

$$k = \frac{E_{interface}}{t_{interface}} \quad (34)$$

In this equation, $E_{interface}$ is the Young's Modulus of the matrix material, and $t_{interface}$ is the thickness of the interface.

An additional element to this linear softening model is friction. Friction is used in this case to prevent slipping regardless of contact pressure. The friction is characterized as rough and once two surfaces contact and undergo rough friction, they should remain closed. This is primarily used with the surface behavior definitions with the no separation option to restrict motions normal to the surfaces. The shear traction slope for this option must also be defined as follows.

$$\text{ShearTractionSlope} = \frac{G_{\text{interface}}}{t_{\text{interface}}} \quad (35)$$

This parameter is used to define a tangential softening in ABAQUS/Explicit.

The second interface model used in this study was a plasticity model. Unlike the linear softening model, it is not a built in function in ABAQUS. Use of this model requires a user subroutine to define the interfacial constitutive relationship. In ABAQUS/Explicit this is known as a VUINTER. The particular user subroutine modeled a uniform thickness interface bonded to both surfaces. This interface material is characterized by uniaxial plasticity in the normal direction with linear hardening, while the shear behavior continues to be elastic. It is also important to note that membrane straining of the interface does not affect the stress being transmitted across the interface. In addition, heat transfer can be incorporated in the form of conductance that is independent of the pressure or gap distance.

The plasticity model requires 7 parameters as shown in Table 1.

Table 1. Plasticity model properties of the interface.

Gap Cut Off	0.000001 m
Young's Modulus	1.797 GPa
Poisson's Ratio	0.42
Initial Yield Stress	16.4 GPa
Hardening Modulus	0.638 GPa
Thickness	0.00001 m
Conductivity	0.1W/m-K

The parameters determined through experimentation were the Young's Modulus and Poisson's Ratio. The remaining parameters such as initial yield stress, hardening modulus, and conductivity were taken from material databases which are a collection of average material properties for various polypropylene types. The data was interpolated to find approximate values for the particular polypropylene used in this study.

The subroutine begins by zeroing and reading in the needed values. Then it is determined whether any two nodes directly across the interface have passed the gap cut off limit. The shear modulus is then computed using the Young's modulus, E , and the Poisson's ratio, ν . This value could just be read in from the material properties, but for simplicity, the program was left as originally written.

$$G = \frac{E}{2(1+\nu)} \quad (36)$$

If the limit has been crossed, the interface at that point is considered separated or debonded, and the stress and heat flux are set to zero, therefore no additional stress or heat transfer can occur. If the two nodes are still bonded, the nominal strain increment, $d\epsilon$, and elastic trial stress, σ_t , are computed as follows. In these equations t is the thickness of the interface and E is the Young's modulus of the

interface and Δt is the relative displacement between the two surfaces. The indices 1, 2, and 3 correspond to 3 dimensions.

$$d\varepsilon_{11} = \frac{\Delta t_1}{t}, d\varepsilon_{12} = \frac{-\Delta t_2}{t}, d\varepsilon_{13} = \frac{-\Delta t_3}{t} \quad (37)$$

$$\begin{aligned} \sigma_{11} &= \sigma_{11} + E * d\varepsilon_{11} \\ \sigma_{12} &= \sigma_{12} + G * d\varepsilon_{12} \\ \sigma_{13} &= \sigma_{13} + G * d\varepsilon_{13} \end{aligned} \quad (38)$$

The next step is to determine how much to scale the normal stress, σ_{11} due to any yielding of the interface. If the absolute value of the elastic trial stress for the normal component is greater than the yield stress, σ_y of the interface then the plastic strain increment is calculated and is shown in equation 39 where E_h is the hardening modulus of the interface.

$$\sigma_t = |\sigma_{11}|, d\varepsilon_{p1} = \frac{\sigma_t - \sigma_y}{E + E_h} \quad (39)$$

The change in yield stress is then calculated using this plastic strain increment.

$$\sigma_y = \sigma_y + E_h * d\varepsilon_{p1} \quad (40)$$

In addition, the corrected normal stress is calculated as follows.

$$\sigma_{11} = \text{sign}(\sigma_y, \sigma_{11}) \quad (41)$$

If an initial temperature of the material is specified in the simulation, along with a thermal conductivity, k , the heat fluxes are calculated using the temperature of the master node, T_{master} , and the temperature of the slave node, T_{slave} .

$$\text{flux} = kA \frac{T_{\text{master}} - T_{\text{slave}}}{t} \quad (42)$$

To conclude the subroutine, if the temperature the particular node being analyzed is equal to or less than zero, the flux is calculated as follows where the master node temperature is taken as that of the first master node.

$$\text{flux} = kA \frac{T_{\text{master}(1)} - T_{\text{slave}}}{t} \quad (43)$$

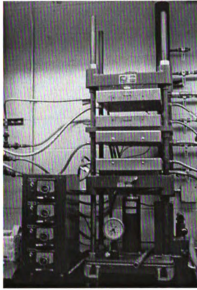
Chapter 2

BACKGROUND

In this study collaboration was done with the Composite Materials and Structures Center at Michigan State University. Researchers in that group have extensive experience fabricating and testing many types of natural fiber composites and expressed an interest in testing the formability of these materials. The material recommended was a Kenaf-Polypropylene composite.

2.1 Fabrication of Kenaf/Polypropylene Composite

In order to fabricate the composites needed for use in the stamping machine, many approaches were used. To begin, the fiber is baked in a vacuum oven for approximately 6 – 8 hours. The fiber is either chopped into pieces 0.197 – 0.315 inches (5 – 8 mm) in length or left long depending on the application. There were two pressing machines used in this study: the Carver Laboratory Press Model SP-F6030 and the Tetrahedron manufactured in San Diego, CA. The Carver press was used for fabrication of smaller composites, while the Tetrahedron had a larger platen and computerized, making it easier to fabricate the larger composites.



(a)



(b)

Figure 2. (a) Carver Press (b) Tetrahedron Press.

The first approach consisted of fabricating 2 – 0.022 lb (10 g) PP sheets and sandwiching 0.019 lb (8.5 g) of long and chopped Kenaf fibers between these sheets. A 5" x 7" x 0.039" inch (127 x 177.8 x 1 mm) stencil was used to ensure proper sizing of the sample.

The second approach was to premix chopped Kenaf fibers and PP powder in a kitchen mixer, prior to pressing. It was observed during the mixing process that most of the PP powder would not distribute evenly through the fiber, but tend to fall to the bottom of the bowl. An attempt was made to do hand mixing in order to more evenly distribute the fiber with little improvement. In order to preserve the 30% fiber composition of the composite, the same amount of fiber and matrix materials was used. The resulting composites from both approaches are shown in Figures 3 - 5.



Figure 3. Long Kenaf fibers sandwiched between two PP sheets.



Figure 4. Chopped Kenaf fibers sandwiched between two PP sheets.



Figure 5. Premixed chopped Kenaf fibers and PP.

As shown, these methods created many voided areas. In the final attempt to produce a more even fiber distribution the PP was changed to the Microfine Polyolefin Powder and a multilayered sprinkling and sifting method was used. The new process is outlined in detail in the following flow chart.

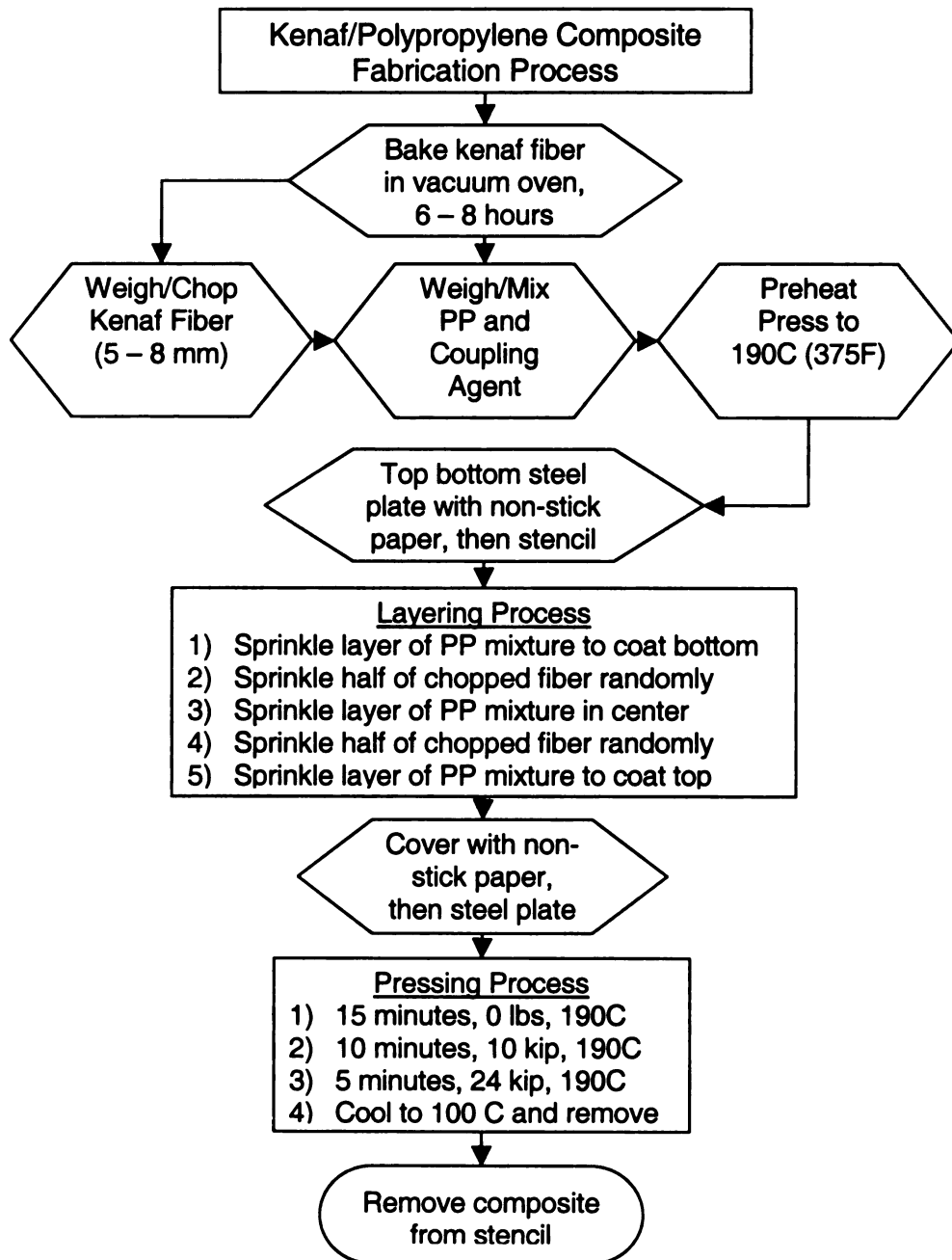


Figure 6. Multilayered composite fabrication process.

The number of layers in the final composites fabricated for material characterization and stamping was contingent upon how many layers were needed in the completed laminate. For example, two layers would consist of three layers of PP, and two layers of fiber. The composite was then pressed using the same process and the resulting composites are shown below.



Figure 7. Multilayered fabricated composite.

It is important to note that the preceding samples were all done with unbaked raw fiber with no surface treatment. In order to make useable samples for stamp thermo-forming process, a coupling agent was introduced in the form of a powder added to the PP powder before fabrication. The coupling agent was Epolene Wax G-3015P from the Eastman Chemical Company in Kingsport, Tennessee. The purpose of the coupling agent is to make the fiber more compatible with the matrix and to provide better adhesion of the matrix to the fiber.

Another improvement to the composites was seen when the fiber was pre-baked in a vacuum oven at 86°F (30°C) for a minimum of 4 hours. It was found

that after baking the fiber would lose approximately 30% of its mass by weight. The extraction of this moisture reduced some of the kink in the fiber, and made it straighter for better chopping. In addition, it allowed for better adhesion between the fiber and the matrix, which can be damaged if water is present. After baking, the fibers, which were originally chopped using scissors, were chopped using a paper cutter. This allowed for better chopping consistency that produced a more even length of fiber.

For the stamping process, a 6.5-7" (165.1 – 177.8 mm) diameter sample was created by using the 8" (203.2 mm) square stencil and using a band saw to cut the circles, followed by sanding the edges with a belt sander to ensure that the edges did not get caught in the die during forming. The individual mass amounts calculated for the 8" inch (203.2 mm) square stencil of 0.079 inch (2 mm) thickness was calculated to be 0.154 lb (69.83 g) of PP, 0.069 lb (31.27 g) of fiber, and 0.007 lb (3.13 g) of coupling agent. For the 12" square stencil of 3 mm thickness, which was used for cutting all material samples for testing, the masses were calculated to be 0.505 lb (229.14 g) of PP and 0.231 lb (104.7 g) of fiber, with 0.023 lb (10.5 g) of the coupling agent.

2.2 Material Characterization - Directionality

To begin characterization of the composite, the first test conducted was a squeeze flow test [27]. The purpose of this test was to determine preferred fiber orientations (in angles) to be used in the tensile testing and simulation. This was done by constructing 3 large 12" double layered composites, which were then cut into 3" circles using a drill press. The zero direction was marked on each sample and it corresponded to the zero direction on the stencil when each composite layer was fabricated. The center was also clearly marked for identification. A sample is shown below.



Figure 8. Squeeze flow test sample before testing.

A schematic of the squeeze flow experimental setup is shown in Figure 9. Prior to testing, the presses were heated to 375 °F (190 °C). The squeeze flow samples were placed between metal plates and then placed into the presses under nominal pressure and allowed to heat for forty minutes. After that time, the platens were compressed to a pressure of 12,000 lbs (53.4 kN) for sixty seconds. The samples were then removed and allowed to cool in the metal plates.

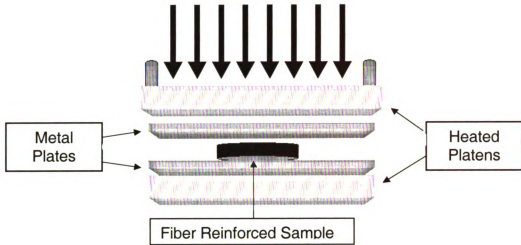


Figure 9. Schematic of squeeze flow test experimental setup [27].

After all 24 samples were pressed; they were labeled in increments of 10 degrees going completely around the sample starting with the zero direction as shown in Figure 10. This was done so that measurements could be taken at each increment to determine in which directions the fibers tended to spread the most.

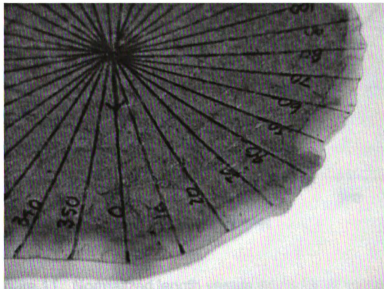


Figure 10. Squeeze flow test sample after testing.

Each sample was then analyzed in two different ways. First, at each angle increment a measurement in millimeters was taken from the center to the edge. Second, the same measurement was taken from the center but excluding the edge areas with large PP concentrations and no fiber. The preferred fiber orientations correspond to the peaks or valleys in the graphs of the measurements. The initial four angles chosen were 40°, 170°, 250°, and 340° degrees. In order to confirm the accuracy of these results; a few of the samples (i.e. 2, 3, 9, 10, 17, and 22) were taken out due to the fiber clumping during testing. The normalized charts for all samples and only the best samples are shown below with the preferred fiber orientations represented by the vertical lines on each graph.

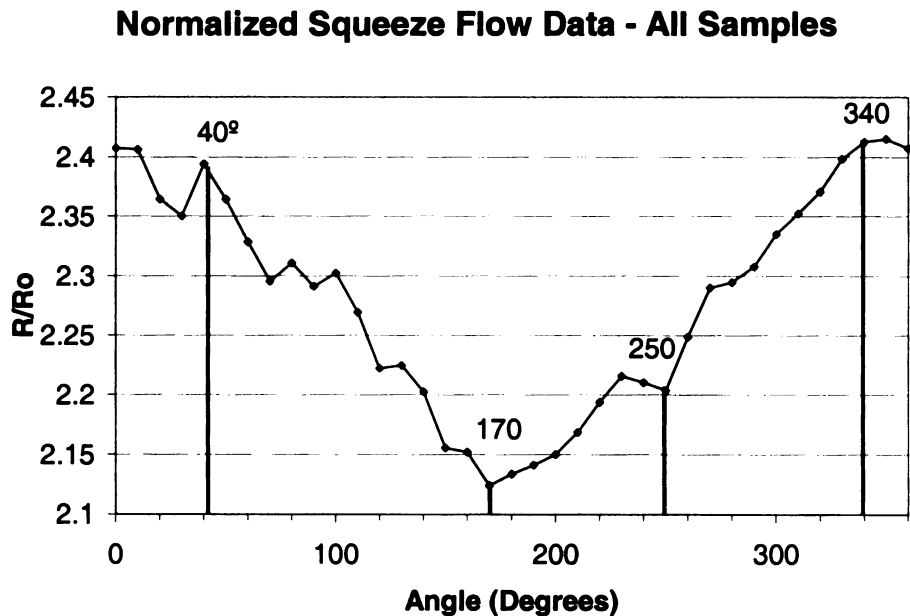


Figure 11. Normalized length versus angle for all samples.

Normalized Squeeze Flow Data - Best Samples

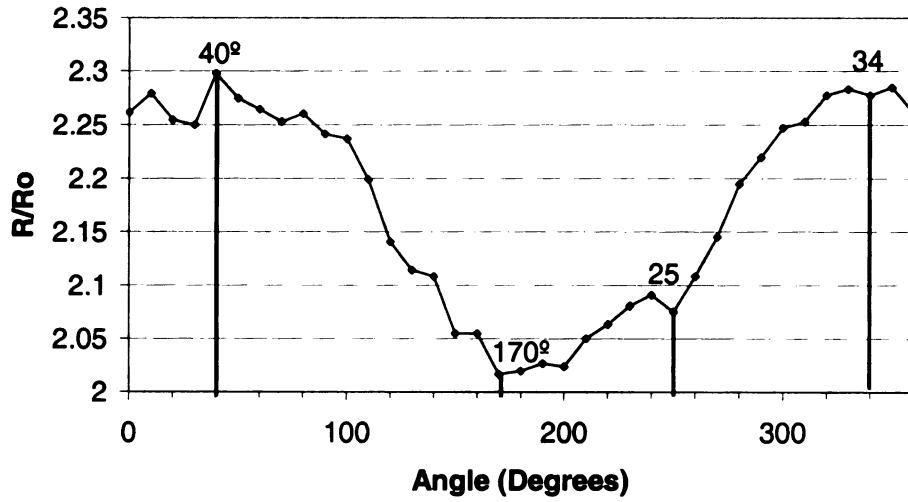


Figure 12. Normalized length versus angle for best samples.

2.3 Material Characterization - Properties

In this study, material characterization has two primary parts – characterization of the composite and characterization of the matrix/interface material – polypropylene. To begin, testing was done at room temperature to determine the tensile properties, i.e. Young's Modulus and Poisson's ratio of the material. The tests were performed on the UTS Machine, Model SFM 20 of United Calibration Corporation, with the twin screw loaded frame.

The standard used was ASTM Standard D638. The required minimum length and width of each specimen was 6.5" (165.1 mm) and 0.5" (12.7 mm), respectively. Two of the preferred fiber orientation angles were used in testing – 40° and 170° degrees, since the two preferred fiber orientation VUMAT was initially chosen to be used in the simulation. Test specimens were cut in each of these directions for testing. In addition, a sheet of PP with Epolene (coupling agent) was made at the same volume ratio as the composite, i.e. 3% coupling agent. A sample of each is shown in Figure 13.



Figure 13. Kenaf/PP and PP tensile specimens.

The testing consisted of two tests for each type of sample. The first procedure exerted a tensile force on the specimens until breakage. This was used to determine the Young's Modulus and other important values. The resulting stress strain curves are shown in Figures 14 - 16. In addition, the average values for the Young's Modulus and other values are shown in Table 2.

Stress-Strain Curve for Kenaf/PP Composites - 40 Degrees

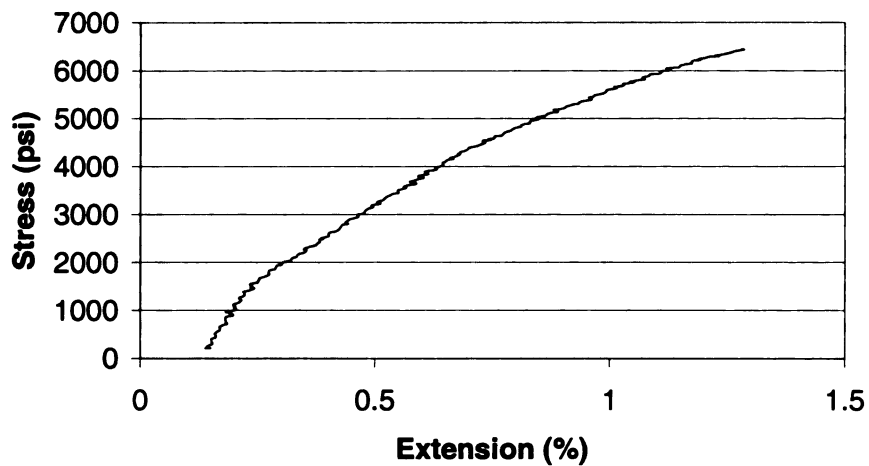


Figure 14. Stress strain curve for 40° fiber orientation specimens at room temperature.

Stress-Strain Curve for Kenaf/PP Composites - 170 Degrees

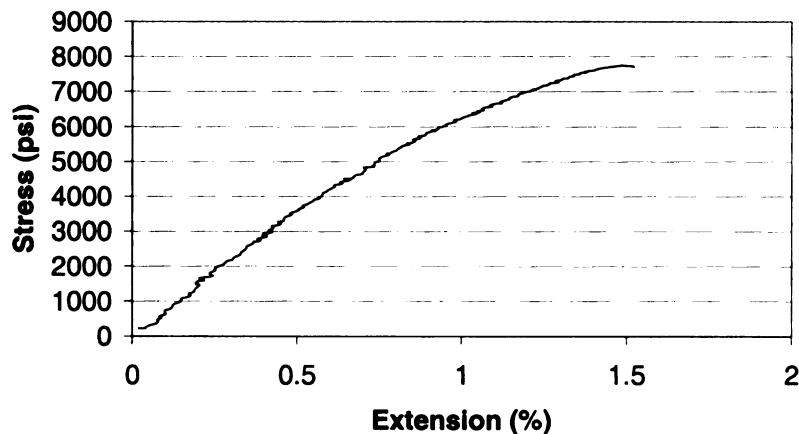


Figure 15. Stress strain curve for 170° fiber orientation specimens at room temperature.

Stress-Strain Curve for Polypropylene/Epolene

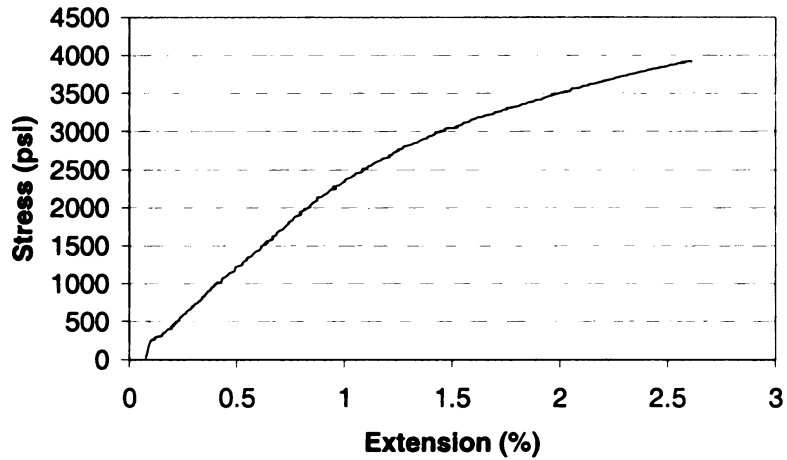


Figure 16. Stress strain curve for Polypropylene/Epolene specimens at room temperature.

It is important to note that from these curves, the behavior of the material is not linear and appears to have some plasticity or viscous properties. For this study, the material model was predetermined. In the future the material behavior could play an important part in the future material model chosen for simulation. In addition, the Young’s Modulus was calculated using the extension range of approximately 0.25 – 0.85 %.

Table 2. Tensile testing results for all specimens – Young’s Modulus.

Specimen Type	Tensile (lbs)	Tensile Strength (psi)	Modulus of Elasticity (psi)	Break Elongation (%)	Tensile Elongation (%)
40 ^o	519.9325	6595.15	592134.4	1.435	1.42
170 ^o	512.88	7263.87	701258.25	1.594	1.57
PP	223.08	4017.468	263036.6	2.752	2.748

In the second procedure, the specimens were only allowed to extend 0.5 in. (12.7 mm). This was done to protect the strain gauges being used to

determine the Poisson's Ratio of the composites and polypropylene. The results are shown in Table 3.

Table 3. Tensile testing results for all specimens – Poisson's Ratio.

Specimen Type	Poisson's Ratio	Tensile (lbs)	Tensile Strength (lbs)	Modulus of Elasticity (psi)	Break Elongation (%)
40°	0.35	496.552	6825.21	773300	0.538
170°	0.4	507.29	5676.35	659594	0.528
PP/Epolene	0.42	223.132	3961.54	313886	0.538

Testing showed a large Poisson's ratio for the PP/Epolene mixture. The normal value for polypropylene without a coupling agent would be around 0.1. This further shows that adhesive strength of the coupling agent. It not only binds the fiber and matrix in the composite, it also adds strength to the matrix material alone.

In addition to tensile testing, a flex test was done using ASTM standard D790 to determine flexural properties and other properties associated with composite performance. This test utilizes a three-point loading system applied to a simply supported beam that subjects the composites to a mixture of tension, compression, and shear forces. The specimens used for these tests were very small with minimum dimensions of 0.5 inches (12.7 mm) and 2.5 inches (63.5 mm) for width and length, respectively. The minimum thickness of each sample was approximately 0.14 inches (3.5 mm). The results are shown in Table 4.

Table 4. Flex testing results for all specimens – Modulus of Elasticity.

Specimen ID	Width (in)	Thickness (in)	Max Force (lbs)	Bend Strength (psi)	MOE (psi)
40°	0.536	0.1424	25.8	8073.4	526814.8
170°	0.5356	0.147	30	8823.6	591062.6

Completed testing gave accurate values of the Young's Modulus and Poisson's Ratio's for two of four preferred fiber orientations, 40° and 170°. The values for the final two preferred fiber orientations, 250° and 340°, were taken as an average of those determined experimentally. Shear modulus values for the fiber were approximated as follows since proper testing methods were not available.

$$G = \frac{E}{2(1 + \nu)} \quad (44)$$

In addition, the Poisson's ratio and shear modulus for the polypropylene were taken from previous work in literature. Values for the transverse shear moduli, G_{13} and G_{23} , were also taken to be 65 kPa [27].

Table 5. Material properties for simulation.

Name	Kenaf/PP	Name	Kenaf/PP
$E_f, 40^\circ$	4.153 GPa	$\nu_f, 340^\circ$	0.375
$E_f, 170^\circ$	4.835 GPa	ν_m, all	0.42
$E_f, 250^\circ$	4.495 GPa	$G_f, 40^\circ$	1.538 GPa
$E_f, 340^\circ$	4.495 GPa	$G_f, 170^\circ$	1.727 GPa
E_m, all	1.797 GPa	$G_f, 250^\circ$	1.63 GPa
$\nu_f, 40^\circ$	0.35	$G_f, 340^\circ$	1.63 GPa
$\nu_f, 170^\circ$	0.40	G_m, all	0.2 MPa
$\nu_f, 250^\circ$	0.375	ν_f	0.384

Table 4. Flex testing results for all specimens – Modulus of Elasticity.

Specimen ID	Width (in)	Thickness (in)	Max Force (lbs)	Bend Strength (psi)	MOE (psi)
40°	0.536	0.1424	25.8	8073.4	526814.8
170°	0.5356	0.147	30	8823.6	591062.6

Completed testing gave accurate values of the Young's Modulus and Poisson's Ratio's for two of four preferred fiber orientations, 40° and 170°. The values for the final two preferred fiber orientations, 250° and 340°, were taken as an average of those determined experimentally. Shear modulus values for the fiber were approximated as follows since proper testing methods were not available.

$$G = \frac{E}{2(1+\nu)} \quad (44)$$

In addition, the Poisson's ratio and shear modulus for the polypropylene were taken from previous work in literature. Values for the transverse shear moduli, G_{13} and G_{23} , were also taken to be 65 kPa [27].

Table 5. Material properties for simulation.

Name	Kenaf/PP	Name	Kenaf/PP
$E_{f, 40^\circ}$	4.153 GPa	$\nu_{f, 340^\circ}$	0.375
$E_{f, 170^\circ}$	4.835 GPa	$\nu_{m, all}$	0.42
$E_{f, 250^\circ}$	4.495 GPa	$G_{f, 40^\circ}$	1.538 GPa
$E_{f, 340^\circ}$	4.495 GPa	$G_{f, 170^\circ}$	1.727 GPa
$E_{m, all}$	1.797 GPa	$G_{f, 250^\circ}$	1.63 GPa
$\nu_{f, 40^\circ}$	0.35	$G_{f, 340^\circ}$	1.63 GPa
$\nu_{f, 170^\circ}$	0.40	$G_{m, all}$	0.2 MPa
$\nu_{f, 250^\circ}$	0.375	ν_f	0.384

2.4 Compression Moulding Process and Composite Comparison

In order to evaluate the effectiveness of the Kenaf/PP composites and the fabrication process previously outlined, a comparison was done to other natural fiber composites. To begin the Kenaf/PP composites made in this study were compared to other compression moulded natural fiber-polypropylene composites with 40% wt. fiber in Figure 17. These composites were fabricated using natural fibers spread between polypropylene films [2]. The Kenaf/PP composites fabricated using the fabrication process used in this study outperformed all fibers with the exclusion of hemp. The properties of the composites improved by introducing the optimized fabrication technique and the addition of the coupling agent, which proves that better matrix fiber adhesion was achieved allowing the composite to reach its full capabilities. In addition, the Kenaf/PP composites fabricated in this study showed a tensile strength of within 725.10 psi (5 MPa) of the Hemp/PP composites found in literature. This was a good achievement considering the fact that hemp fiber alone has a tensile strength of 79.77 – 130.53 ksi (550-900 MPa) while Kenaf ranges from only 41.19 – 116.03 ksi (284-800 MPa) [2,12].

Tensile Strength Comparison of Compression Moulded Composites

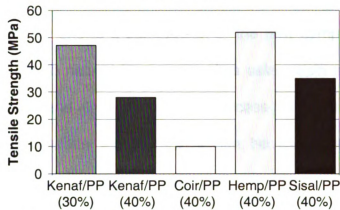


Figure 17. Tensile strength comparison.

The flexural strength of the Kenaf/PP composites in this study were also compared with previous results from other compression moulding studies [2]. The new process has produced nearly double the flexural strength of some other natural fiber composites, including other Kenaf/PP composites. The exception to this gain was once again the Hemp/PP composites. Yet, it is believed that Hemp/PP composites produced with the new technique would outperform these layered hemp composites [2].

Flexural Strength Comparison of Compression Moulded Composites

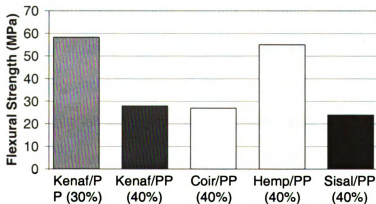


Figure 18. Flexural strength comparison.

A comparison was also done between the compression moulding process and other manufacturing processes that are currently in use to fabricate composites. Figure 19 shows a comparison of the new compression moulded Kenaf/PP composites to natural fiber composites using resin transfer moulding [13], and an extrusion and injection moulding process [14]. Although fiber types and weights differ between the studies, it can be concluded that the new optimized compression moulding process is a very competitive manufacturing process.

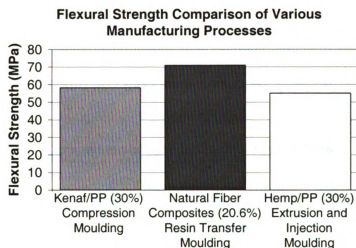


Figure 19. Flexural strength comparison for various manufacturing processes.

Using the elastic modulus data from the material testing, it is possible to compare the benefits of using this Kenaf composite over other natural fibers as well as E-glass. In Figures 20 and 21, it is shown that the Kenaf/PP composites in this study have a higher Modulus/Cost and Specific Modulus than sisal, coir, and E-glass fibers. Therefore, not only has Kenaf been proven to be a viable replacement for more expensive and non-biodegradable glass fibers, the new

optimized fabrication process has been proven to produce competitive composites to those already in use.

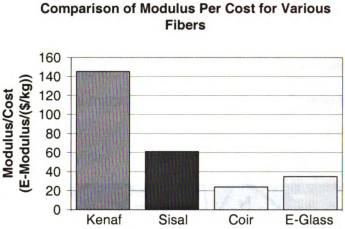


Figure 20. Modulus per cost comparison.

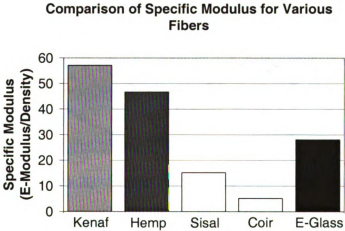


Figure 21. Specific modulus comparison.

Chapter 3

EXPERIMENTAL WORK

3.1 Introduction to Stamp Thermoforming

Experimental stamping simulations were used in evaluating the accuracy of the numerical results. The machine used was a stamp thermo-hydroforming press pictured below.



Figure 22. Stamp thermo-hydroforming press.

The press consisted of a 4 in. (101.6 mm) hemispherical punch to form the parts with a female die. Nothing was used to constrict movement of the sheets as they were formed in order to see the wrinkling behavior. A gap of 0.6 in. (15.24 mm) was maintained between the blank holder and the die. The samples were drawn

to a depth of 1.47 in (37.338 mm) and allowed to partially cool before being removed. A schematic is also shown to illustrate each part of the press.

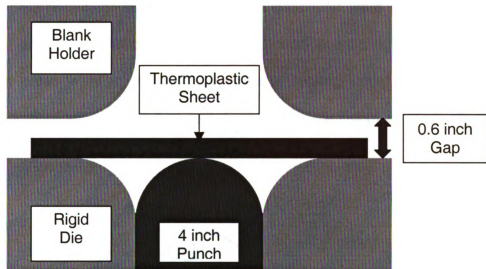


Figure 23. Stamp thermoforming schematic.

Initially the bottom die portion was heated to approximately 350°F (177°C), which was measured using a thermocouple. The samples were also preheated in an oven to the same temperature for approximately 20 minutes. This allowed for better forming and melting of the polypropylene without burning the natural fibers.

3.2 Experimental Stamping Results

In order to form parts properly numerous samples were fabricated and tested. The parameters for stamping previously described were the optimized values found from trial and error. Initially, it was found that during fabrication, if any resin rich areas were in the initial samples, a tearing would occur during forming. In addition, some of the first samples tested were not preheated, which also led to tearing. A sample of this is shown below.



Figure 24. Stamp thermoformed part with tearing - top view.

Therefore, care was taken in fabrication so resin rich areas did not occur. The following parts were successfully formed using the stamping press.



(a)



(b)

Figure 25. Stamp thermoformed part A, (a) top view, (b) side view.



(a)



(b)

Figure 26. Stamp thermoformed part B, (a) top view, (b) side view.

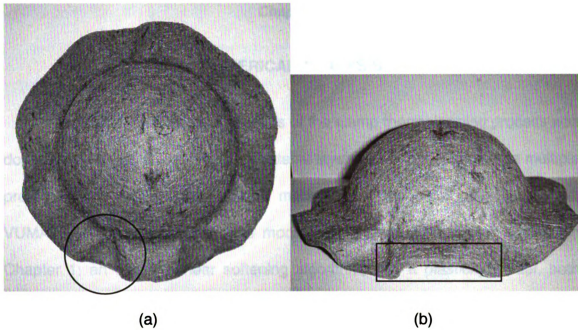


Figure 27. Stamp thermoformed part C, (a) top view, (b) side view.

It is important to note the similarities amongst all these formed samples. To begin, the top view of each part shows that the material forming is asymmetric. In addition, each part consistently formed 7 wrinkles. The wrinkles were not very round (or wave like), but rectangular from the side view, which can be seen in the rectangular outline in Figure 27(b). In addition, there are parts in the wrinkling that exhibit a pinching effect and form triangular corners as shown in the circled outline in Figure 27(a). Also, no separation of the layers was seen. These behavioral similarities are what will be used in the comparison to the numerical simulations.

Chapter 4

NUMERICAL ANALYSIS

The complete numerical analysis of the stamp thermoforming process was done using ABAQUS/Explicit. The material layers were modeled using a multiple preferred fiber orientations updated material law through a user subroutine, VUMAT. The interface layer was modeled using two methods as outlined in Chapter 1: an existing linear softening algorithm, and a plasticity model, both used in ABAQUS.

4.1 Material Model

The constitutive relationship used in this study was developed by Mike Zampaloni et al and is based on preferred fiber orientations [27]. These orientations can be non-orthogonal, and are determined using squeeze flow testing as outlined in Chapter 2. The approach is to model the fiber-reinforced material as unidirectional layers. Each layer is considered independently and a stiffness matrix is created with the summation of all these layers. This model used an updated material law which took into account the fact a material's constitutive relationship changes with deformation.

The stiffness matrix [Q] is determined based on its principal geometrical axes. This is done for each preferred fiber direction.

$$[Q_{ij}] = \begin{bmatrix} Q_{11} & Q_{12} & Q_{13} \\ Q_{21} & Q_{22} & Q_{23} \\ Q_{31} & Q_{32} & Q_{33} \end{bmatrix} \quad (45)$$

In this equation, the subscript 6 was changed to 3 for simplicity. Since each layer is very thin, a plane stress assumption was used. The components of the stiffness matrix can be written in terms of the engineering constants as shown in equations 46 through 51.

$$Q_{11} = \frac{E_{11}}{(1 - \nu_{12}\nu_{21})} \quad (46)$$

$$Q_{22} = \frac{E_{22}}{(1 - \nu_{12}\nu_{21})} \quad (47)$$

$$Q_{12} = \frac{\nu_{12}E_{11}}{(1 - \nu_{12}\nu_{21})} \quad (48)$$

$$Q_{33} = G_{12} \quad (49)$$

$$Q_{13} = Q_{31} = Q_{23} = Q_{32} = 0 \quad (50)$$

$$Q_{21} = Q_{12} \quad (51)$$

In these equations, E_{11} represents the Young's Modulus in the 1-direction and E_{22} is the Young's Modulus normal to the 1-direction. The Poisson's Ratio and the Shear Modulus in the 1-direction are ν_{12} and G_{12} , respectively. For any other preferred fiber orientation, the same directions hold. Therefore, E_{11} is the Young's Modulus in the fiber direction, E_{22} is the Young's Modulus in the matrix normal to the fiber direction, and ν_{12} and G_{12} are the Poisson's Ratio and Shear Modulus in the fiber direction.

Since the material properties are measured along the fiber directions, they must be transformed into the material frame to assure continuity. The transformation matrix is shown in equation 41, where Θ is the angle between the

material frame and the fiber directions. The m is the cosine of θ and n is the sine of θ . The final constitutive relation for a single fiber orientation is shown in equation 53.

$$T(\theta) = \begin{bmatrix} m^2 & n^2 & 2mn \\ n^2 & m^2 & -2mn \\ -mn & mn & m^2 - n^2 \end{bmatrix} \quad (52)$$

$$[\sigma]_k = \begin{bmatrix} \bar{Q}_{11} & \bar{Q}_{12} & \bar{Q}_{13} \\ \bar{Q}_{21} & \bar{Q}_{22} & \bar{Q}_{23} \\ \bar{Q}_{31} & \bar{Q}_{32} & \bar{Q}_{33} \end{bmatrix}_k [\mathcal{E}]_k \quad (53)$$

For multiple preferred fiber orientations, a combined stiffness matrix is created to take into account the behavior in all the directions.

$$[\bar{Q}]_{\text{sheet}} = [\bar{Q}]_1 + [\bar{Q}]_2 + \dots + [\bar{Q}]_n \quad (54)$$

$$[\sigma] = [\bar{Q}]_{\text{sheet}} [\mathcal{E}] \quad (55)$$

This constitutive relationship was implemented through a user subroutine, VUMAT, in an ABAQUS/Explicit analysis. Three versions of the VUMAT were used in this study: 2, 3, and 4 preferred fiber orientations.

4.2 Numerical Stamping Results

4.2.1 – Two Preferred Fiber Orientations

Initially, the two preferred fiber orientation VUMAT was used in conjunction with both interface models. Many factors were found to affect the quality and validity of the simulation including mesh size, punch velocity, and total simulation time. The mesh was reduced from 12800 TRIA elements for each layer (2 total) to 5712 QUAD elements, and finally to 2723 TRIA elements. This drastically reduced computation time and file size for each simulation. In addition to the change in mesh, the velocity curve was changed to a triangular shape. Since the simulation is a quasi-static process, there were a few things that needed to be considered.

Applying ABAQUS/Explicit to a quasi-static problem required special considerations. By definition a static solution is over a long period of time, but that can be impractical when it comes to simulation. The long time period would require an excessive number of small time increments. In order to counteract this dilemma, it is imperative to model the process in the shortest time period in which the inertial forces remain insignificant [28].

This is achieved by changing loading rates, using smooth amplitude curves, and even in some instances using mass scaling. The loading rate can be increased so the event occurs in less time as long as dynamic effects remain insignificant. A smooth amplitude curve may also be used. If there are sudden movements they can induce noise which will lead to an inaccurate solution. It was found in this study that the best amplitude curve was triangular, which

allowed for the velocity to steadily increase and then decrease to the finish. Another important factor is mass scaling. ABAQUS has a built in mass scaling function that can be used either as *FIXED MASS SCALING or *VARIABLE MASS SCALING. The same result can be accomplished by artificially increasing the material density, although care must be taken to not increase the density too much or an inaccurate solution will also occur. The minimum stable time increment of all elements can be expressed as follows.

$$\Delta t = \frac{L^e}{c_d} \quad (56)$$

In this equation, L^e is the characteristic element length and c_d is the dilation wave speed of the material, which is given by the following equation where E is the Young's Modulus and ρ is the material density.

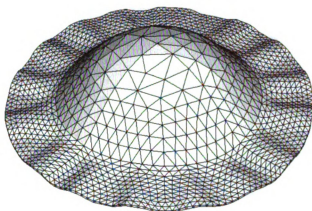
$$c_d = \sqrt{\frac{E}{\rho}} \quad (57)$$

Therefore, if the density is increased by a factor of f^2 then the wave speed decreases by a factor of f , and the stable time increment increases by a factor of f . This leads to fewer increments required to perform the analysis, thus decreasing the time of the simulation.

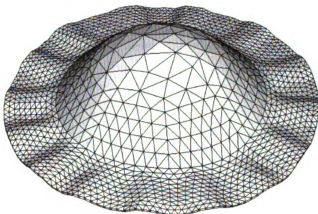
In conclusion, under the assumption that a quasi-static analysis in real time would be virtually the same as a completely static solution, it is often necessary to change simulation parameters such as loading rate, mass, and amplitude in order to achieve an accurate simulation. In this study, the velocity was modeled to ensure that the internal energy leveled off, and the kinetic

energy gradually increased then decreased to the end. The total time also played a role in the simulation, not only for computational time, but to achieve the best model of the quasi-static process.

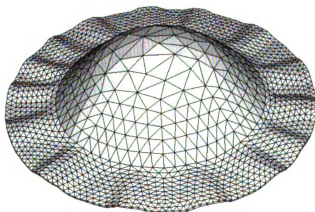
Initially, the initial volume fraction was under scrutiny. Using the density of 87.40 lb/ft³ (1.4g/cc), the volume fraction was calculated to be 0.218. Upon visual observation of the composite, this number seemed to be very low compared to the large volume of fiber put into each composite sheet. Therefore, a density test was done on the fiber. The fiber was put in a glass of water to see if it floated. Since the fiber did float, it was determined that perhaps the density was actually less than 62.43 lb/ft³ (1 g/cc), the density of water. Therefore, after a literature search, it was found that the density of cubed Kenaf fiber is 55.56 lb/ft³ (.89 g/cc) which gave an initial volume fraction of 0.384 [15]. In order to test the sensitivity of the initial volume fraction, simulations were done with 0.218, 0.384, and 0.6. In addition, the Poisson's ratio was taken to be 0.2, 0.3, and 0.4 as another sensitivity test. For this sensitivity analysis, only the linear softening model was used, which only used two of the material parameters. The results are shown below in Figures 28 to 30. It is important to note the differences in each simulation. Very little changes were noticed when varying the Poisson's ratio or volume fraction as shown.



(a)

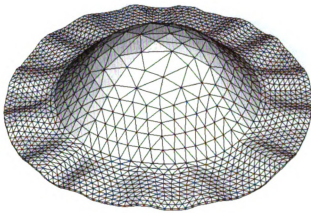


(b)

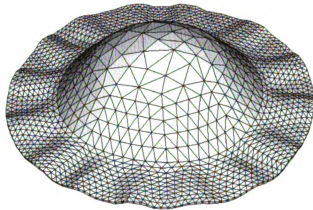


(c)

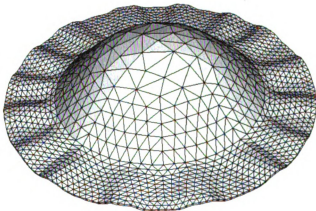
Figure 28. Deformed blank for $v=0.2$ (a) $V_f=0.218$ (b) $V_f=0.384$ (c) $V_f=0.6$.



(a)

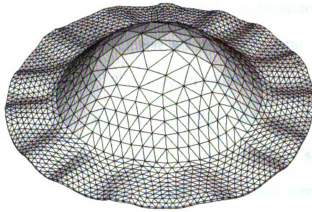


(b)

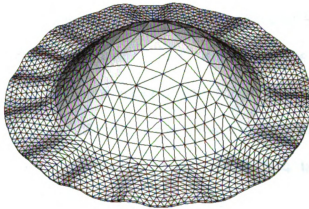


(c)

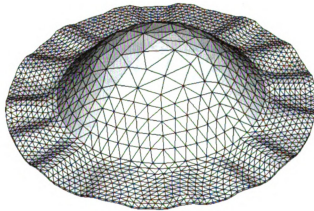
Figure 29. Deformed blank for $v=0.3$ (a) $V_f=0.218$ (b) $V_f=0.384$ (c) $V_f=0.6$.



(a)



(b)



(c)

Figure 30. Deformed blank for $v=0.4$ (a) $V_f=0.218$ (b) $V_f=0.384$ (c) $V_f=0.6$.

From initial observation, 15 wrinkles were associated with each blank, which is double an actual part. Unlike actual results, the wrinkles appeared evenly spaced around the part. The only Poisson's ratio that showed a slight difference was 0.3 with a volume fraction of 0.384. In Figure 29 (b) the deformed part has 15 wrinkles, but less material is found on one side of the formed hemisphere than the other, similar to the behavior when forming. Therefore, it was determined that a Poisson's ratio of 0.3 was a key value, which is corroborated by the tensile testing results that show Poisson's ratios of 0.35 and 0.4. The volume fraction chosen was 0.384. In addition, the plasticity interface model was used in a simulation in order to see if there were any changes. The result is shown in Figure 31. Similar to the linear softening interface, this model was unable to capture the behavior found during experimentation. Therefore, it was determined that the two preferred fiber orientation was insufficient, and work began on the three and four preferred fiber orientation VUMAT's.

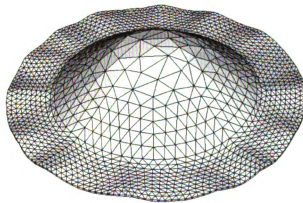


Figure 31. Deformed blank for $\nu=0.3$ and $V_f=0.384$ with a plasticity model interface.

4.2.2 – Three Preferred Fiber Orientations

The program for three preferred fiber orientations used the same constitutive model as before, but with an extension for the third fiber direction. Since the sensitivity analysis was already done, the Poisson's ratio was set to 0.35, 0.4, and 0.375 for the 40°, 170°, and 250° fiber directions, respectively. The initial volume fraction was set to .384. Difficulty arose when using the 250° preferred fiber orientation, therefore 70° was used instead since the results for the squeeze flow show symmetry from 0° – 180° and 180° – 360°. The resulting deformation is shown below.

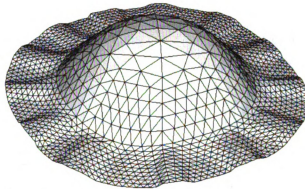


Figure 32. Deformed blank for 3 preferred fiber orientations VUMAT.

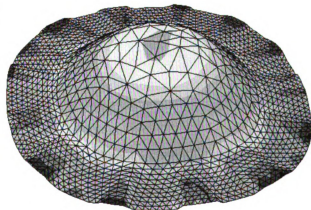
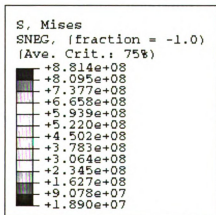
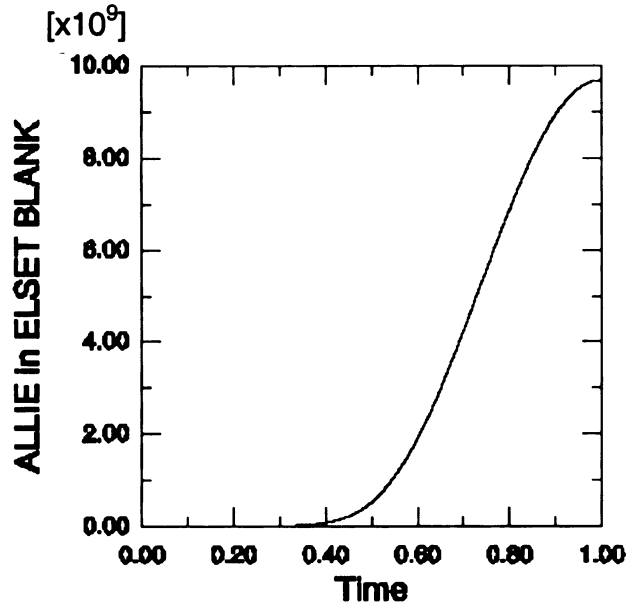
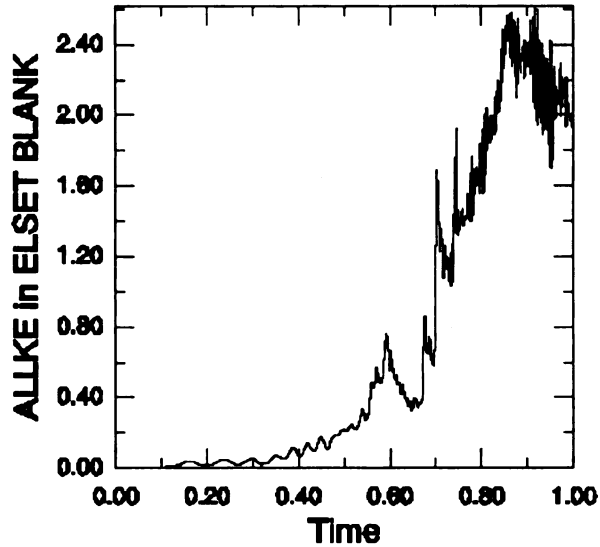


Figure 33. Stress contour plot for 3 preferred fiber orientations VUMAT.



(a)



(b)

Figure 34. Internal (a) and Kinetic (b) energy plots for 3 preferred fiber orientations VUMAT.

An important observation of the deformed part in Figure 32 is that there are 13 wrinkles. This is fewer than with the 2 preferred fiber orientations, but still

almost double the amount found in the actual formed part. The internal and kinetic energy both show good quasi-static behavior.

4.2.3 – Four Preferred Fiber Orientations

The program for four preferred fiber orientations again used the same constitutive model as before, but with an extension for the third and fourth fiber directions. The Poisson's ratio was set to 0.375 for the new direction and the initial volume fraction to .384. The resulting deformation is shown below.

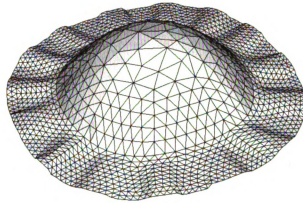


Figure 35. Deformed blank for 4 preferred fiber orientations VUMAT.

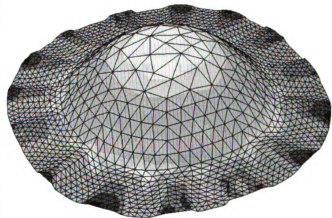
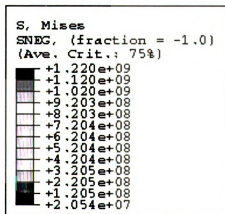
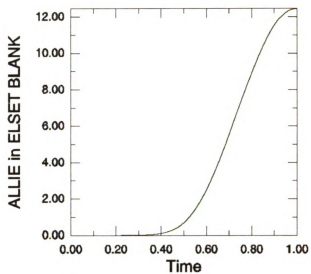
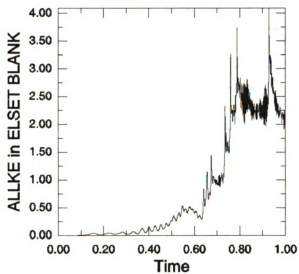


Figure 36. Stress contour plot for 4 preferred fiber orientations VUMAT.



(a)



(b)

Figure 37. Internal (a) and Kinetic (b) energy plots for 4 preferred fiber orientations VUMAT.

This simulation again showed 15 wrinkles as with the two preferred fiber orientations. The internal and kinetic energy are also acceptable. Since previously for the two preferred fiber orientations a sensitivity analysis was done for the volume fraction and Poisson's ratio, one was also conducted on the three and four preferred fiber orientation models. This time the analyzed parameter was the Young's Modulus. The following table shows the results of this analysis.

Table 6. Sensitivity analysis of Young's Modulus.

Young's Modulus of Fiber Directions – 3PFO	% Complete	# of Wrinkles
$E=E*10^7$	85	12+
$E=E*10^8$	85	12+
$E=E*10^9$	100	15
$E=E*10^{10}$	100	23+
$E=E*10^{11}$	100	∞
Young's Modulus of Fiber Directions – 4PFO	% Complete	# of Wrinkles
$E=E*10^7$	100	13
$E=E*10^8$	100	13-14
$E=E*10^9$	100	15
$E=E*10^{10}$	90	27+
$E=E*10^{11}$	100	∞

The results show that as the Young's Modulus is decreased, the number of wrinkles decrease, and vice versa. Yet, they do not decrease enough to match the actual formed part. Therefore, it was determined that for a Young's modulus between an order of the 7th to 9th power, there is not a lot of change in the simulation. For higher powers, the simulation becomes unstable.

4.3 Discussion of Results

The results of the simulations were somewhat different than the experimental results. To begin this analysis a picture of different view of the simulations versus the actual experiments are shown below.

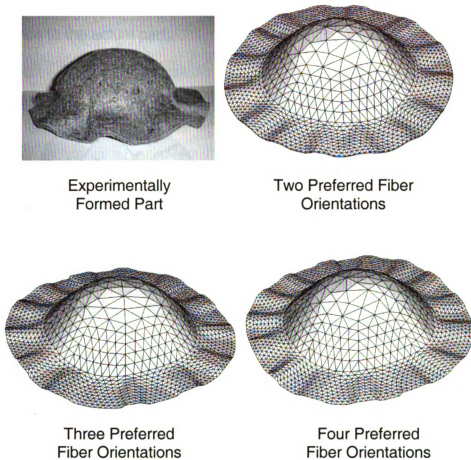


Figure 38. Front angled views of formed part and simulations.

The results do not show a good correspondence between the wrinkling behavior of the experimentally formed parts and the simulations. Where the experimental part only has 7 wrinkles, the simulated parts have 15 wrinkles, nearly double. The two preferred fiber orientation model used with the linear

softening showed the most unusual behavior. It was highly asymmetric, and had one half of the formed part with more material on that side than the other, which is usually how the actual part formed. Yet, the 3 and 4 preferred fiber orientations didn't show this behavior. In addition, the wrinkles tended to be flatter and wider than the 2 preferred fiber orientations model. This is more of a resemblance to the actual part.

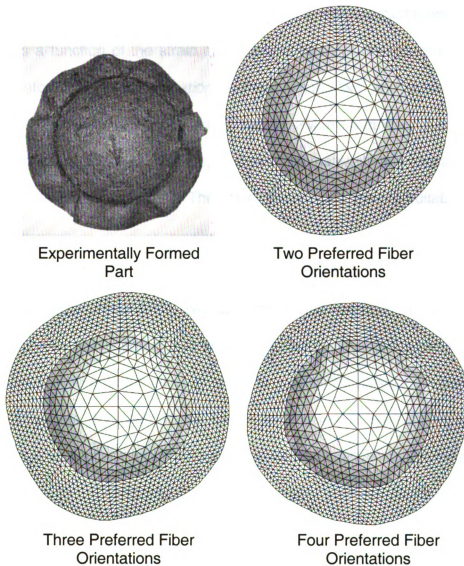


Figure 39. Top views of experimental and simulation results.

The top views further show the asymmetry of the parts. Yet, it is not an exact replica of what was found in experiment. One reason for this could have been the fact that the updated material law model uses a constitutive relationship with linear elastic stress-strain relations. By definition, an elastic material is one that returns to its original (unloaded) shape once the applied forces are applied. This type of elastic behavior is before permanent deformation. In this case a more suitable model may be a viscoelastic material. In a viscoelastic material the state of stress is a function of the strain and the time rates of change of the strain as well. Therefore it uses a combination of elastic (spring-like) and viscous (dashpot-like) elements to form a viscous-elastic model. Many materials such as glass, ceramics, plastics, synthetic rubbers, and even biomaterials are considered to be linear viscoelastic materials [29]. Therefore, this may be a more suitable model to use.

In 2000, Klasztorny et al derived a viscoelastic model for unidirectional fibrous polymeric composites. The composite was modeled as a viscoelastic isotropic polymer matrix and elastic monotropic fibers. The Mittag-Leffler fractional exponential functions were used in order to model the shear/bulk creep in the matrix. Therefore, the viscoelastic model for the matrix was described with 2 elastic and 6 viscoelastic constants and the elastic fibers were described with 5 elastic constants. Collectively both models were used to derive the coupled constitutive equations and the composite together was modeled as a homogeneous monotropic material with 5 elastic constants, and 27 viscoelastic constants (i.e. 9 long lasting compliance ratios, 9 retardation times, and 9 fractions

defining the order of the fractional exponential functions). This study also provides a way to theoretically predict the viscoelastic constants [30].

In addition, Holzapfel et al used a viscoelastic model for a fiber-reinforced composite material that exhibits direction-dependent properties and sustain finite strains without a significant volume change. The composites used were made of a soft matrix material reinforced by two different types of fibers, or two fiber directions. Like the model used in this study, a global response is given by a summation of all individual responses of the material. This work developed a closed-form expression for the fourth-order elasticity tensor. Constitutive models were presented for special cases including orthotropic, transversely isotropic, and isotropic hyperelastic materials at finite strains with and without dissipation. The model was validated using 2D and 3D simulation results and comparing those to experimental results of a pressurized laminated circular tube, which has a strong anisotropic response [31]. This is considered to be on a macro mechanical or continuum approach.

Additional works on viscoelastic constitutive models on a microscopic level were done by R. M. Haj-Ali and A. Muliana in 2004. The approach was to idealize each unidirectional lamina using the Aboudi four-cell micro model. This is coupled with incremental formulation in interfaces of the average stress and strain in each sub cell. The matrix sub cells are described by the Scharpery non-linear viscoelastic model and the fiber is considered transversely isotropic and linear elastic. The sub cell constitutive relationships are embedded in a numerical stress-update algorithm. This framework can easily include temperature, moisture,

and physical aging effects. It was implemented within a shell-based non-linear finite element analysis by assuming plane stress. The formulation was validated using several experimental off-axis specimen creep tests and was applied to a laminated panel and a composite ring, both showing agreement [33].

The time dependent response of polymeric composite systems was studied using classical homogenization methods in 2002 by Sejnoha and Zeman. The study focused on random, non-periodic material systems with loading that promotes the viscoelastic deformation of the material. Two modeling approaches were used. In the first, the material was represented using volume elements with a small number of particles to statistically represent the microstructure of the composite. These elements are periodically dispersed and a finite element analysis can be carried out. The second approach is based on the Hashin-Shtrikman variational principles. The randomness of the fiber is incorporated using statistical descriptors. This work was only applicable to microstructures that can be described by the two-point probability function [34].

Overall, it is possible that any of these methods could be used in place of the current, elastic representation. In addition, the processing temperature of the composite could have an effect on its behavior. It has been shown in a recent study of ramie fibers, another natural fiber, that processing temperatures between 180 – 200 °C for a given period of time can cause degradation of the mechanical properties of exposed fibers [6]. Since the melting temperature of the polypropylene is approximately 160°C and the composites are fabricated and formed at 190°C it will melt during forming and possibly expose fibers to the

temperature degradation. This can be remedied by surface modification of the natural fibers, which also improves the mechanical properties [6].

Another important issue to consider is the moisture absorption of the fiber. Natural fibers, such as Kenaf, are hydrophilic which means they absorb water. An average range of moisture absorption is 5 – 10% although in some cases it has been reported to be as high as 20% (~30% was found in this study). This moisture can affect the final properties of the composite once it is processed by creating voids between the fiber and the matrix which can interfere with the fiber/matrix adhesion [13].

In addition, the preferred fiber orientations can be taken into account. The method used selected at most four preferred fiber orientations, and measurements were only taken at every 10 degrees. A more accurate representation may be found by taking measurements every 2 – 5 degrees and by using an Orientation Distribution Function (ODF). This would allow for a multi-orientation approach and could prove to capture the behavior of this material more accurately.

Furthermore, the Young's modulus of the fiber is on the same order as the matrix. The updated material law model was originally built based on representing the matrix as an elastic material, which was adequate because of the higher strength of the glass fibers. Therefore, the fibers controlled the behavior and material properties of the composite. In the Kenaf/polypropylene composites used in this study, the Young's modulus of the fiber is the same order of magnitude as the matrix. Therefore, a more accurate model for the matrix material, which is not

elastic, should be used. This is another reason a different material model such as viscoelastic or viscoplastic should show better results.

In conclusion, any of these affects could have led to poor representation during simulation. A viscoelastic model could prove to be a better representation of the material behavior. Additionally, fiber treatment could be done that would not only increase the overall strength and properties of the fibers, but will also keep them from absorbing moisture and experiencing degradation during processing. In addition, the use of an ODF may also more accurately capture the material behavior.

Chapter 5

CONCLUSIONS

In the present work, an optimized process for the fabrication of Kenaf natural fiber and polypropylene composites has been presented. This process proved to provide good adhesion between the fiber and matrix. In addition, an evenly dispersed fiber distribution was achieved. The composites also showed comparable tensile and flexural strength with other natural fiber and polypropylene composites fabricated by compression moulding and other fabrication processes.

In addition, simulations were performed using ABAQUS/Explicit with a VUMAT (user defined material constitutive relationship) coupled with a VUINTER (user defined interface model) in an attempt to represent experimental forming of the composites. The numerical simulations did not show good resemblance. Possible reasons for the discrepancies include the use of an elastic constitutive relationship and the addition of a coupling agent into the polypropylene powder instead of fiber treatment. The stress-strain curves from tensile testing clearly show non-linear behavior. Therefore, a viscoelastic constitutive model could prove to be more appropriate. Additionally, fiber treatment would not only help keep the fibers from being damaged during heat processing, it would also decrease the moisture absorption of the fibers, further improving the consistency and performance of the composites. Furthermore, the use of an ODF would allow for a multi-orientation representation of the material.

Chapter 6

FUTURE WORK

There are many options for future work with the kenaf and polypropylene composites presented in this study. These include but are not limited to the varying of the fiber volume fraction and using fiber treatment instead of adding the coupling agent to the polypropylene powder. In addition, more testing could be completed including tensile testing at elevated temperatures and Dynamic Mechanical Analysis (DMA) testing for further characterization.

Numerical work could include the use of different material model – possibly viscoelastic, or one that is found to more closely resemble the actual behavior of the composite material. In addition, different interface models can be incorporated. The linear softening and plasticity models could be used with a different material model or any of the models presented in literature could be substituted. Also, the use of an ODF could improve the simulations representation of the actual material behavior.

Additional work could also use the sandwiching of the kenaf and polypropylene sheets with a metal such as aluminum.

BIBLIOGRAPHY

COMPOSITE MATERIAL CHARACTERIZATION

1. Mohanty, A.K., Drzal, L.T., and Misra, M. "Novel hybrid coupling agent as an adhesion promoter in natural fiber reinforced powder polypropylene composites." Journal of Materials Science Letters 21(2002): 1885-1888.
2. Wambua, P., Ivens, J., and Verpoest, I. "Natural fibres: can they replace glass in fiber reinforced plastics?" Composites Science and Technology 63(2003): 1259 – 1264.
3. Feng, D., Caulfield, D.F., and Sanadi, A. R. "Effect of Compatibilizer on the Structure-Property Relationships of Kenaf-Fiber/Polypropylene Composites." Polymer Composites 22(2001): 506 – 517.
4. Joshi, S. V., Drzal, L. T., Mohanty, A. K., and Arora, S. "Are natural fiber composites environmentally superior to glass fiber reinforced composites?" Composites: Part A 35 (2004): 371 – 376.
5. Mohammad, P., and Sain, M. M. 'Sheet-Molded Polyolefin Natural Fiber Composites for Automotive Applications.' Macromolecular Materials and Engineering 288(2003): 553 – 557
6. Mohanty, A.K., Misra, M., and Hunrichsen, G. "Biofibres, biodegradable polymers and biocomposites: An overview." Macromolecular Materials and Engineering 276/277 (2000): 1-24.
7. Mohanty, A.K., Drzal, L.T., and Misra, M. "Engineered natural fiber reinforced polypropylene composites: influence of surface modifications and novel power impregnation processing." J. Adhesion Sci. Technol., 16 (2002): 999 - 1015.
8. Biagiotti, J., Fiori, S., Torre, L., Lopez-Manchado, M. A., and Kenny, J. M. "Mechanical Properties of Polypropylene Matrix Composites Reinforced With Natural Fibers: A Statistical Approach." Polymer Composites, 25(2004): 26 – 36.
9. Nishino, T., Hirao, K., Kotera, M., Nakamae, K., Inagaki, H. "Kenaf reinforced biodegradable composites." Composites Science and Technology 63 (2003): 1281 – 1286.
10. Karian, Harutun G. Handbook of Polypropylene and Polypropylene Composites. New York: Marcel Dekker, Inc., 1999.

11. Chung, T. C. Mike. Functionalization of Polyolefins. New York: Academic Press, 2002.
12. Mohanty A.K., Misra M., and Drzal L.T... "Sustainable Bio-Composites from Renewable Resources: Opportunities and Challenges in the Green Materials World." Journal of Polymers and the Environment 10(2002): 19 - 26.
13. Rouison, D., Sain, M., and Couturier. M. "Resin transfer molding of natural fiber reinforced composites: cure simulation." Composites Science and Technology 64(2004): 629 – 644.
14. Mohanty, A.K., Wibowo, A., Misra, M., and Drzal, L.T. "Effect of process engineering on the performance of natural fiber reinforced cellulose acetate biocomposites." Composites Part A: Applied Science and Manufacturing 35(2004): 363 – 370.
15. Webber III, Charles L., Bledsoe, V.K., and Bledsoe, R. E. "Kenaf Harvesting and Processing." Trends in New Crops and New Uses (2002): 340 – 347.

DELAMINATION

16. Zou, Z., Reid, S.R., and Li, S. "A continuum damage model for delaminations in laminated composites." Journal of the Mechanics and Physics of Solids 51 (2003): 333-356.
17. Alfano, G., and Crisfield, M.A. "Finite element interface models for the delamination analysis of laminated composites: mechanical and computational issues." International Journal for Numerical Methods in Engineering 50 (2001): 1701-1736.
18. Hillerborg, A., Modeer, M., and Petersson, P.E. "Analysis of crack formation and crack growth in concrete by means of fracture mechanics and finite elements." Cement and Concrete Research 6(1976): 773 – 782.
19. Dugdale, D.S. "Yielding of steel sheets containing slits." Journal of the Mechanics and Physics of Solids 8 (1960): 100 – 104.
20. Borg, R., Nilsson, L., and Simonsson, K. "Simulation of delamination in fiber composites with a discrete cohesive failure model." Composites Science and Technology 61 (2001): 667-677.

21. Wells, G.N., and Sluys, L.J. "A new method for modeling cohesive cracks using finite elements." International Journal for Numerical Methods in Engineering 50(2001): 2667 – 2682.
22. Espinosa, H.D., Dwivedi, S., and Lu, H.C. "Modeling impact induced delamination of woven fiber reinforced composites with contact/cohesive laws." Computer Methods in Applied Mechanics and Engineering 183(2000): 259 – 290.
23. Blackman, B. R. K., Hadavinia, H., Kinloch, A.J., and Williams, J.G. "The use of a cohesive zone model to study the fracture of fibre composites and adhesively-bonded joints." International Journal of Fracture 119(2003): 25 – 46.
24. Borg, R., Nilsson, L., and Simonsson, K. "Simulation of low velocity impact on fiber laminates using a cohesive zone based delamination model." Composites Science and Technology 64(2004): 279 – 288.
25. Bruno, D., Greco, F., and Lonetti, P. "A coupled interface-multilayer approach for mixed mode delamination and contact analysis in laminated composites." International Journal of Solids and Structures 40(2003): 7245 - 7268.
26. Corigliano, A. and Ricci, M. "Rate-dependent interface models: formulation and numerical applications." International Journal of Solids and Structures 38(2001): 547 – 576.
27. Zampaloni, M.A., A multi-preferred fiber orientation constitutive model for fiber mat reinforced thermoplastics with a random orientation applied to the stamp thermo-hydroforming process. Michigan State University, 2003.
28. Hibbit, Karlsson & Sorensen Inc. ABAQUS Manuals. 2004.
29. Ugural, Ansel C. and Fenster, Saul K. Advanced Strength and Applied Elasticity Third Edition. Upper saddle River, NJ: Prentice Hall, 1995.
30. Klasztorny, M. and Wilczynski, A. P. "Constitutive Equations of Viscoelasticity and Estimation of Viscoelastic Parameters of Unidirectional Fibrous Polymeric Composites." Journal of Composite Materials 34(2000): 1624 – 1639.
31. Holzapfel, G. A., and Gasser, T. C. "A viscoelastic model for fiber-reinforced composites at finite strains: Continuum basis, computation aspects and applications." Computer Methods in Applied Mechanics and Engineering 190(2000): 4379 – 4403.

MICHIGAN STATE UNIVERSITY LIBRARIES



3 1293 02732 4882